LBNL-56895

Strategies for Detecting Hidden Geothermal Systems by Near-Surface Gas Monitoring

Jennifer L. Lewicki

Curtis M. Oldenburg

Earth Sciences Division
Ernest Orlando Lawrence Berkeley National Laboratory
Berkeley, CA 94720

December 15, 2004

This work was supported by the Assistant Secretary for Energy Efficiency and Renewable Energy, Office of Geothermal Technologies, of the U.S. Department of Energy, and by the Office of Science, U.S. Department of Energy, under Contract No. DE-AC03-76SF00098.

DISCLAIMER

TABLE OF CONTENTS

LIST OF TABLES

LIST OF FIGURES

This page left intentionally blank.

ABSTRACT

"Hidden" geothermal systems are those systems above which hydrothermal surface features (e.g., hot springs, fumaroles, elevated ground temperatures, hydrothermal alteration) are lacking. Emissions of moderate to low solubility gases (e.g., CO_2, CH_4, He) may be one of the primary near-surface signals from these systems. Detection of anomalous gas emissions related to hidden geothermal systems may therefore be an important tool to discover new geothermal resources. This study investigates the potential for CO_2 detection and monitoring in the subsurface and above ground in the near-surface environment to serve as a tool to discover hidden geothermal systems. We focus the investigation on CO_2 due to (1) its abundance in geothermal systems, (2) its moderate solubility in water, and (3) the wide range of technologies available to monitor CO_2 in the near-surface environment. However, monitoring in the near-surface environment for CO_2 derived from hidden geothermal reservoirs is complicated by the large variation in CO_2 fluxes and concentrations arising from natural biological and hydrologic processes.

In the near-surface environment, the flow and transport of CO_2 at high concentrations will be controlled by its high density, low viscosity, and high solubility in water relative to air. Numerical simulations of CO_2 migration show that CO_2 concentrations can reach very high levels in the shallow subsurface even for relatively low geothermal source CO_2 fluxes. However, once CO_2 seeps out of the ground into the atmospheric surface layer, surface winds are effective at dispersing CO_2 seepage.

In natural ecological systems in the absence of geothermal gas emissions, near-surface CO_2 fluxes and concentrations are primarily controlled by CO_2 uptake by photosynthesis, production by root respiration, and microbial decomposition of soil/subsoil organic matter, groundwater degassing, and exchange with the atmosphere. Available technologies for monitoring CO_2 in the near-surface environment include (1) the infrared gas analyzer (IRGA) for measurement of concentrations at point locations, (2) the accumulation chamber (AC) method for measuring soil CO_2 fluxes at point locations, (3) the eddy covariance (EC) method for measuring net CO_2 flux over a given area, (4) hyperspectral imaging of vegetative stress resulting from elevated CO_2 concentrations, and (5) light detection and ranging (LIDAR) that can measure CO_2 concentrations over an integrated path. Technologies currently in developmental stages that have the potential to be used for CO_2 monitoring include tunable lasers for long distance integrated concentration measurements and micro-electronic mechanical systems (MEMS) that can make widespread point measurements.

To address the challenge of detecting potentially small-magnitude geothermal CO_2 emissions within the natural background variability of CO_2, we propose an approach that integrates available detection and monitoring methodologies with statistical analysis and modeling strategies. Within the area targeted for geothermal exploration, point measurements of soil CO_2 fluxes and concentrations using the AC method and a portable IRGA, respectively, and measurements of net surface flux using EC should be made. Also, the natural spatial and temporal variability of surface CO_2 fluxes and subsurface CO_2 concentrations should be quantified within a background area with similar geologic, climatic, and ecosystem

characteristics to the area targeted for geothermal exploration. Statistical analyses of data collected from both areas should be used to guide sampling strategy, discern spatial patterns that may be indicative of geothermal CO_2 emissions, and assess the presence (or absence) of geothermal CO_2 within the natural background variability with a desired confidence level. Once measured CO_2 concentrations and fluxes have been determined to be of anomalous geothermal origin with high confidence, more expensive vertical subsurface gas sampling and chemical and isotopic analyses can be undertaken. Integrated analysis of all measurements will determine definitively if CO_2 derived from a deep geothermal source is present, and if so, the spatial extent of the anomaly. The appropriateness of further geophysical measurements, installation of deep wells, and geochemical analyses of deep fluids can then be decided based on the results of the near surface CO_2 monitoring program.

1. INTRODUCTION

Most commercial geothermal projects have been developed near previously known resources, for example, near hot springs or areas of historic use. Also, the majority of hydrothermal systems with obvious surface expressions in the U.S. have already been explored for geothermal development potential. Discovery of new geothermal systems will therefore require exploration of areas where the reservoirs are either hidden or lie at greater depths than presently known reservoirs. As a result, research must be geared toward the development of novel exploration techniques to locate these new geothermal resources.

Here, we define "hidden" geothermal systems as those systems above which hydrothermal surface features (e.g., hot springs, fumaroles, elevated ground temperatures, hydrothermal alteration) are lacking. Emissions of moderate to low solubility gases (e.g., CO_2, CH_4, He) may be one of the primary near-surface signals from these systems. Detection of anomalous gas emissions related to hidden geothermal systems may therefore be an important tool to discover new resources (Klusman et al., 2000). We will focus our discussion specifically on the detection and monitoring of CO_2 in the subsurface and above ground in the near-surface environment as a tool to discover hidden geothermal systems because (1) CO_2 is the major non-condensable gas present in geothermal reservoirs (e.g., Ellis and Mahon, 1977), (2) due to its moderate solubility in water, CO_2 from volcanic-hydrothermal sources tends to migrate to the near-surface in the gaseous phase in equal or greater proportion than dissolved in the aqueous phase in groundwater (e.g., Cruz et al., 1999; Favara et al., 2001; Evans et al., 2002), and (3) a broad range of technologies are available to monitor CO_2 in the near-surface environment. Importantly, however, CO_2 is produced in the near surface by a variety of biological processes, and monitoring of CO_2 from hidden geothermal reservoirs will involve monitoring a system with large variation in CO_2 fluxes and concentrations arising from natural biological and hydrologic processes. The detection of anomalous CO_2 will therefore require searching for *potential* geothermal CO_2 anomalies, likely of small magnitude, over areas of tens of km^2 or more within the naturally varying background CO_2 fluxes and concentrations.

The objective of this report is to discuss geothermal CO_2 monitoring in the near surface as a tool to discover hidden geothermal reservoirs. To this end, we present (1) the physical properties of CO_2 key to its transport in the near-surface environment, (2) model simulations of geothermal CO_2 migration and seepage that highlight fundamental features of these processes, (3) a discussion of the processes that affect natural background CO_2 fluxes and concentrations within which anomalous geothermal CO_2 must be discerned, (4) technologies that are currently available or will be potentially available in the future to monitor CO_2 migration and seepage in the near surface, and (5) potential strategies to detect geothermal CO_2 seepage fluxes and concentrations within the naturally varying background fluxes and concentrations.

2. FLUXES AND CONCENTRATIONS OF CO_2 IN KNOWN VOLCANIC AND HYDROTHERMAL SYSTEMS

Over the past several decades, numerous diffuse CO_2 degassing studies have been conducted in known (i.e., "visible") volcanic and hydrothermal environments, many of which focused on characterizing the magnitude and spatial distribution of CO_2 emissions. While surface CO_2 emission rates from hidden geothermal systems will likely be lower than those measured in known volcanic and hydrothermal systems, the preferential pathways for CO_2 flow from depth to the near surface will likely be similar. As discussed below, the magnitudes and styles of diffuse CO_2 emissions vary from site to site. Here, we briefly review the surface CO_2 fluxes and soil CO_2 concentrations measured in these systems. In most cases, the AC method (see section 6.2.2 below) was used to measure surface CO_2 fluxes and the CO_2 concentrations of soil gases were measured using a portable IRGA (see section 6.2) or by laboratory gas chromatography.

At Solfatara crater, Campi Flegrei caldera, Italy, surface CO_2 fluxes up to 75,000 g $m^{-2}d^{-1}$ were measured (e.g., Cardellini et al., 2003), with average flux estimated to be 1520 g $m^{-2}d^{-1}$ (Chiodini et al., 2001). Elevated fluxes here were primarily focused along faults and fractures. At Vulcano Island, Italy, CO_2 fluxes up to 12,000 g $m^{-2}d^{-1}$ were measured (Cardellini et al., 2003). CO_2 fluxes up to 22,000 g $m^{-2}d^{-1}$ were measured at Poggio dell'Ulivo, an area of cold CO_2 degassing in the Central Italian magmatic province (Cardellini et al., 2003). At the Central American volcanoes of Masaya (Nicaragua), Cerro Negro (Nicaragua), Poas (Costa Rica), and Arenal (Costa Rica), fluxes up to 50,000 (average = 2750, Lewicki et al., 2003), 35,000 (Salazar et al., 2001), 140 (Williams-Jones et al., 2000), and 291 g $m^{-2}d^{-1}$ (Williams-Jones et al., 2000), respectively, were measured. Elevated fluxes at these volcanoes were predominantly measured along eruptive fissures and faults. Koepenick et al. (1996) reported fluxes up to 1350 g $m^{-2}d^{-1}$ (average = 166 g $m^{-2}d^{-1}$) near fumaroles and fractures on Oldoinyo Lengai volcano, Tanzania, whereas Hernandez et al. (2001) reported fluxes up to 18,150 g $m^{-2}d^{-1}$ at Miyakejima, Japan, mainly focused along flank fissures and on the main volcanic cone. At Mammoth Mountain, USA, average measured CO_2 flux ranged from 1500-2100 g $m^{-2}d^{-1}$, with maximum values of >10,000 g $m^{-2}d^{-1}$ (Gerlach et al., 2001). CO_2 flow here was hypothesized to be controlled by faulting. At the Dixie Valley Geothermal Field, USA, CO_2 fluxes up to 570 g $m^{-2}d^{-1}$ were measured near faults and fumaroles (Bergfeld et al., 2001). Werner et al. (2000) reported CO_2 fluxes up to 30,000 g $m^{-2}d^{-1}$ in the Yellowstone volcanic system, with average fluxes of 89 g $m^{-2}d^{-1}$ in travertine depositing areas to 1200 g $m^{-2}d^{-1}$ in acid-sulfate areas. Elevated fluxes here were mainly focussed along faults and fractures.

Soil CO_2 concentrations measured in volcanic and hydrothermal environments have also varied widely, depending on the study area and proximity to geologic features (e.g., faults, eruptive fissures) influencing gas flow. At Poas volcano, concentrations up to 16 vol.% were measured by Williams-Jones et al. (2000). At Arenal and Galeras (Colombia) volcanoes, Willams-Jones et al. (2000) reported concentrations up to 7.3 and 13 vol.%, respectively. Soil CO_2 concentrations up to 90 vol.% were measured at Oldoinyo Lengai volcano (average = 14 vol.%, Koepenick et al., 1996), Mammoth Mountain (Sorey et al., 1998), and the Yellowstone volcanic system (Werner et al., 2000). Similar to surface CO_2 fluxes, elevated soil CO_2 concentrations were commonly associated with faults, fractures, eruptive fissures, and vents in these study areas.

3. PHYSICAL PROPERTIES OF CO_2 IN THE NEAR SURFACE

Pressures and temperatures in the shallow subsurface (e.g., within the vadose zone and close to the water table) are close to those in the atmosphere near the ground surface. Figure 3.1 shows the density of CO_2-air mixtures as a function of concentration (mole fraction) at three different temperatures (Magee et al., 1994; NIST, 1992) where air is dry and composed of 79% nitrogen (N_2) and 21% oxygen (O_2) by volume. As shown in Figure 3.1, CO_2 has greater density than dry air, and the gases mix approximately ideally at atmospheric pressure. Note that the density contrast between CO_2 and air will be larger in the vadose zone than indicated in Figure 3.1 due to the presence of water vapor with lower density relative to dry air. Figure 3.2 shows that under the same pressure and temperature conditions, CO_2 is less viscous than air (Magee et al., 1994; NIST, 1992).

Figure 3.3 shows the solubility of CO_2 and N_2 (where N_2 is a proxy for air) in water as a function of gas composition (mole fraction) at three different temperatures (Spycher et al., 2003). In these model calculations, the partial pressure of CO_2 is significantly in excess of atmospheric partial pressure. Thus, the pH of the solution is maintained below ~6 and H_2CO_3 is the dominant aqueous carbon species present. Carbon dioxide has greater solubility (approximately 50x) in water than does N_2 (air). The solubility of CO_2 decreases as temperature increases and as its partial pressure decreases. Carbon dioxide gas bubbles are usually formed when CO_2-saturated ground water migrates upwards in the subsurface and pressure decreases.

The transport of CO_2 in the shallow subsurface is also controlled by its molecular diffusivity, which is comparable to that of other components in air (e.g., N_2, O_2, H_2O) and is approximately 1.65×10^{-5} m^2 s^{-1} at 25 °C, 1 bar (Vargaftik et al., 1996). Pressure and temperature have compensating effects on molecular diffusion, as described for solubility; diffusivity tends to decrease as pressure increases with depth and increase with increasing temperature.

In summary, CO_2 is a dense and inviscid gas relative to air. Carbon dioxide will therefore tend to be mobile and sink due to buoyancy effects. However, because CO_2 and other gases in the near surface are fully miscible, no significant density segregation is expected to occur in gas mixtures unless there is relative flow between the gas and liquid water. This flow may cause CO_2 to preferentially dissolve in groundwater and leave behind a gas mixture enriched in the less soluble components. If groundwater pressure decreases and/or temperature increases, exsolution may occur, releasing CO_2 back to the gas phase.

4. SIMULATIONS OF CO_2 MIGRATION

4.1 Introduction

In this section we present numerical simulations of CO_2 migration, seepage, and atmospheric dispersion. The purpose of these simulations is to evaluate the magnitudes and form of anomalous CO_2 concentrations and fluxes that might be expected to emanate from a given model

hidden geothermal system. From this information, we can design and evaluate potential monitoring and detection methods.

4.2 Methods

4.2.1 Introduction

We use the simulator T2CA (Oldenburg and Unger, 2004), a research module of TOUGH2 (Pruess et al., 1999). T2CA retains the fundamental porous media flow and transport capabilities of TOUGH2, and models five components (water, brine, CO_2, a gas tracer, and air) under isothermal or non-isothermal conditions. The main advance in T2CA is the implementation of a simple atmospheric transport and dispersion capability for dilute gases based on variable-K theory (Arya, 1999). In variable-K theory, a constant time-averaged wind velocity profile is specified for advection, and atmospheric dispersion is modeled as a diffusion process with variable diffusivity as a function of height above the ground surface. In this way, T2CA models coupled subsurface and atmospheric surface layer gas flow and transport. Because the subsurface methods in TOUGH2 are well documented and described elsewhere (e.g., Pruess et al., 1999), we focus here on describing briefly the atmospheric dispersion methods, for which more detail can be found in Oldenburg and Unger (2004).

4.2.2 Logarithmic Velocity Profile

The ambient time-averaged wind profile near the ground surface follows a logarithmic profile (e.g., Slade, 1968, p. 73). The logarithmic wind profile is valid over approximately the lower one-tenth of the atmospheric boundary layer, or approximately a few tens of meters above the ground surface. The logarithmic wind profile as shown on Figure 4.1 is given as:

$$u(z) = \frac{u*}{k} \ln\left(\frac{z}{z_0}\right) \tag{4.1}$$

where $u(z)$ is the ambient wind velocity as a function of height above the ground surface, u_* is the friction velocity (a parameter that governs the shape of the wind profile near the ground surface for various surface types), k is von Karman's constant ($k = 0.4$), z is the elevation, and z_0 is a roughness height that is a function of various surface types and for which $u(z) = 0$ for $z \leq z_o$ (Slade, 1968). The logarithmic wind profile is strictly applicable to neutral stability conditions.

4.2.3 Advective-Dispersive Transport

The mean turbulent transport of CO_2 as a passive gas in the surface layer can be described by the advective-dispersive transport equation with variable eddy diffusivities (K_x, K_y, K_z) (Arya, 1999, p. 137). For the three-dimensional (x, y, z) transport of a component (e.g., CO_2) at concentration c, this equation is

$$\frac{\partial c}{\partial t} + u\frac{\partial c}{\partial x} + v\frac{\partial c}{\partial y} + w\frac{\partial c}{\partial z} - \frac{\partial}{\partial x}\left(K_x \frac{\partial c}{\partial x}\right) - \frac{\partial}{\partial y}\left(K_y \frac{\partial c}{\partial y}\right) - \frac{\partial}{\partial z}\left(K_z \frac{\partial c}{\partial z}\right) = 0 \tag{4.2}$$

For convenience in surface-layer transport modeling, the coordinate system can be arranged so that x is aligned in the downwind direction, making $v = w = 0$ where u is the ambient wind. We assume that the seeping gas concentration is low enough that it does not affect the velocity field, i.e., we make a dilute gas assumption.

4.2.4 Dispersion Model

For the special case of constant eddy diffusivities and a uniform wind velocity (u) with no shear (i.e., no velocity gradient), and assuming that advection dominates diffusion in the x-direction, solutions to Eq. 4.2 are given by the well-known Gaussian plume dispersion model, with constant eddy diffusivities D_{xx}, D_{yy}, and D_{zz} given by

$$D_{xx} = \frac{\sigma_x^2}{2t},\ D_{yy} = \frac{\sigma_y^2}{2t},\ D_{zz} = \frac{\sigma_z^2}{2t} \tag{4.3}$$

where σ_x, σ_y, σ_z are the standard deviations of concentration distributions at an observation or receptor point, and t is the travel time to the point (e.g., Arya, 1999, p. 132).

Although attractive for its simplicity and widely used in pollutant transport applications, the Gaussian plume model is not valid for situations with wind shear (i.e., a non-zero gradient of u with height), as appropriate for winds near the ground surface that affect CO_2 seepage (Arya, 1999, p. 197-199). Theory and data point to the need for variable eddy diffusivities (K_x, K_y, K_z), an approach called variable-K theory. The variable-K theory is recommended for cases with wind shear and non-homogeneous turbulence such as will be found in the surface layer (Arya, 1999, p. 143). For our surface-layer applications involving CO_2 seepage, we have used variable K-theory and the assumption that K_z increases linearly with height as

$$K_z = k\ u_*\ z \tag{4.4}$$

(Arya, 1999, p. 143). This model assumes neutral stability in the surface layer, allows for a variable wind speed with height, and models the larger dispersion that occurs as the plume moves upward. Because there is no analogous formulation of K_y (transverse dispersion) valid for short travel distances (< 10 km) in variable-K theory (Arya, 1999, p. 151), we adopt here a 2-D configuration for our test problem that models only vertical dispersion and downwind advection. Because CO_2 dispersion will occur only in the vertical direction, this represents a conservative model in that actual CO_2 concentrations downwind will be lower for emissions from any realistic areal source for which lateral dispersion occurs. The neglect of lateral dispersion is not an inherent limitation of T2CA, which is in fact three-dimensional, and can include lateral dispersion assuming a reasonable parameterization is available.

In summary, T2CA uses a logarithmic velocity profile and variable-K theory to model multicomponent gaseous (CO_2, gas tracer, and air) transport in a 2-D surface layer that is directly coupled with a porous medium subsurface region. In this approach, we calculate eddy diffusivities from the variable-K diffusivity of Eq. 4.4 to produce an effective atmospheric dispersivity at every gridblock in the surface layer, a convenient approach in the discretized framework of T2CA. Although it is normally negligible in the surface layer, the molecular diffusion coefficient is added to the eddy diffusivity with the largest term controlling the

dispersion process. The single effective dispersivity is then used in the advective-dispersive transport equation for each chemical component to model surface-layer transport.

4.2.5 Limitations

In general, CO_2 dispersion can occur either as a dense or a passive gas, depending on the local CO_2 concentration. Our approach is applicable only to passive gas transport in the surface layer (Oldenburg and Unger, 2004). Therefore, this approach is applicable only to cases of small CO_2 seepage flux in which the ambient winds are not affected by CO_2 seepage. This assumption is easily met for windy conditions and for the small seepage fluxes expected from hidden geothermal systems.

Time-averaged winds are assumed in the logarithmic velocity profile, and no account is made of daily changes in winds, temperature, or weather. We assume the time scale of interest is on the order of 1 mo. to 10 years, time scales over which averaging is defensible. Length scales for mixing are on the order of 10 m to 1 km.

Numerical dispersion in the implicit and upstream-weighted TOUGH2 framework is on the order of one-half the grid spacing multiplied by the velocity. Because of the alignment of the grid with the unidirectional wind, numerical dispersion occurs only in the flow direction (i.e., x-direction) in the surface layer. In the quasi-steady cases we are considering, advection dominates transport in the flow direction. In the vertical direction, the velocity is zero ($w = 0$). Thus, vertical eddy diffusion is unaffected by numerical dispersion. If CO_2 front tracking in the surface layer ever arises as a focus of interest, special weighting schemes can be implemented to diminish numerical dispersion in the flow direction (e.g., Oldenburg and Pruess, 2000).

4.3 Conceptual Model

The geologic framework of the model hidden geothermal system we consider is based loosely on an arid basin and range system like the Dixie Valley geothermal system (e.g., Benoit, 1999; McKenna and Blackwell, 2004), only without any surface manifestations. In particular, we consider a model in which a growing alluvial fan covers a geothermal anomaly created by deep range-bounding faults so that it is essentially invisible at the surface. Within this system, we model the migration of CO_2 upward from a small (15 m^2) region that represents the top of a conductive fault, located near the water table. The CO_2 spreads in the heterogeneous system as it migrates upward until it seeps out at the ground surface. A conceptual model of the system is shown in Figure 4.2, along with the outline (dashed) of the model domain. We present results from the start of CO_2 migration up to 200 years, at which point the gas seepage flux and concentrations are nearly steady. The grid and boundary conditions for the subsurface region are shown in Figure 4.3. The grid consists of 67 15-m gridblocks in the x-direction, and 31 4-m gridblocks in the z-direction, with the grid tilted at six degrees. We do not consider the effects of infiltration of meteoric water to simplify models and focus attention on arid basin and range-type environments. Additional properties of the system are presented in Table 4.1.

We consider both a homogeneous permeability case, along with five realizations of heterogeneous permeability. The heterogeneous permeability cases are significant because gas migration will tend to follow high-permeability pathways. We present in Figure 4.4 five realizations (referred to as realizations A–E) of a heterogeneous permeability field generated

using simulated annealing to represent an alluvial fan deposit (note the vertical exaggeration). The permeability is characterized by a mean value of 10^{-12} m^2, and varies by four orders of magnitude. There is a 45-m correlation length in the *Y*-direction (sub-horizontal), and no correlation in the vertical direction, thereby creating a layered structure intended to represent an alluvial fan.

4.4 Results

4.4.1 Subsurface Migration

We simulated the subsurface migration of CO_2 from a 15 m^2 source area near the water table at three different source strength rates (q_{CO2} = $1x10^{-6}$, $1x10^{-5}$ and $1x10^{-4}$ kg s^{-1}, Table 4.1). These rates are equivalent to source CO_2 fluxes of 5.76, 57.6 and 576 g m^{-2} d^{-1}, respectively, when normalized by the source emission area. These CO_2 fluxes were arbitrarily chosen to produce small CO_2 seepage fluxes, and are significantly lower (i.e., up to four orders of magnitude) than surface CO_2 fluxes measured in known/visible volcanic and hydrothermal systems. While we do not know the range of source CO_2 fluxes that will be expected from a hidden geothermal system, we chose to model this low range of values to test the capability limits of available technologies for near-surface CO_2 detection. For reference, the largest source CO_2 flux we consider is similar to the highest surface CO_2 fluxes measured at the Dixie Valley Geothermal Field, Nevada (Bergfeld et al., 2001). First, to illustrate the two-dimensional flow behavior of CO_2 in the subsurface, we present the results for high source CO_2 flux (576 g $m^{-2}d^{-1}$) and heterogeneous subsurface permeability (realizations A-E). To illustrate the expected near-surface CO_2 signals for the purpose of detection analysis (see Sections 6 and 7), we then present one-dimensional horizontal profiles of shallow subsurface CO_2 concentrations and surface CO_2 fluxes associated with the three source strengths for (1) homogeneous subsurface permeability and (2) heterogeneous permeability (realizations A-E). To facilitate comparison of CO_2 concentration results, 1 vol% = 10^{-2} mole fraction = 10^4 ppmv. The initial condition for the simulations is a static unsaturated-saturated system as shown in Figure 4.5 by the liquid saturation fields.

The CO_2 plume after 0.5, 1, and 10 years of migration for the homogeneous permeability case is presented in Figure 4.6. As shown, CO_2 migrates upward and outward from the source and reaches the ground surface in approximately one year. Results for heterogeneous systems (heterogeneity realization A) are presented in Figure 4.7. As shown, there is a slight preferential migration in the sub-horizontal direction reflecting the permeability structure of the alluvial fan. However, the plume seeps out of the ground after only slightly more than one year. As observed in prior work (Oldenburg and Unger, 2003), at late times (after 10 years) the CO_2 concentration in the shallow subsurface can become very high even though the CO_2 flux is quite small. CO_2 plumes after 200 years of migration for permeability realizations A-E are shown in Figure 4.8. At 200 years, the CO_2 plumes for the different permeability fields are similar in general shape and CO_2 concentration distribution.

Figure 4.9 shows the horizontal profiles of CO_2 concentration at 3 m depth and surface CO_2 flux associated with a subsurface with homogeneous isotropic permeability and low, medium, and high source CO_2 source fluxes (t = 200 years). These profiles all show a similar smooth increase and then decrease in concentration and flux crossing the CO_2 plume. Maximum CO_2

concentrations for the low, medium, and high source strengths are about 2 x 10^4, 1 x 10^5 and 6 x 10^5 ppmv, respectively, whereas maximum surface CO_2 fluxes are about 2 x 10^{-4}, 0.2, and 40 g m^{-2} d^{-1}, respectively. These profiles also show that the width of the CO_2 plume increases with increasing source strength. If the source area of CO_2 emission were increased (i.e., to simulate more diffuse, rather than focused CO_2 flow), the magnitude of the near-surface CO_2 concentration and flux signals would decrease, while the width of the anomaly would increase.

Profiles of CO_2 concentration at 3 m depth and surface CO_2 flux associated with a subsurface with heterogeneous permeability (realizations A-E) and low CO_2 source flux (t = 200 years) are shown on Figure 4.10. Figures 4.11 and 4.12 present results for medium and high CO_2 source strengths, respectively. At low source flux, CO_2 concentration profiles associated with the heterogeneous permeability realizations are broadly similar to those associated with homogeneous permeability. In other words, both heterogeneous and homogeneous permeability profiles display a similar relatively smooth increase then decrease in concentration across the plume maximum concentrations (although these concentrations vary somewhat between realizations A-E) and similar width of the CO_2 anomaly. For profiles corresponding to the low source flux and both homogeneous and heterogeneous permeabilities, the CO_2 concentrations at 3 m depth fall within the range of natural background CO_2 concentrations arising from biological processes (see Section 7.2.1). At medium and high source fluxes, the concentration profiles for heterogeneous permeability realizations A-E diverge from profiles associated with homogeneous permeability, showing greater spatial variability of concentrations. These changes are likely due to an increasing contribution of advective transport of CO_2 through relatively high permeability pathways at elevated source fluxes. For all source CO_2 fluxes, profiles of surface CO_2 fluxes associated with heterogeneous permeability differ from those associated with homogeneous permeability at the same source strengths. Relative to the homogeneous permeability cases, fluxes along the heterogeneous profiles are more spatially variable and maximum observed fluxes may be greater or less, depending on the presence of high or low permeability pathways, respectively.

4.4.2 Surface-Layer Dispersion

In this section, we present results of the coupled subsurface-surface layer system to investigate above-ground CO_2 concentrations for the model system. The methods in T2CA assume a horizontal ground surface, above which a constant logarithmic wind profile exists. To accommodate this assumption, we simulated a horizontal system rather than the tilted system used for the subsurface simulations discussed in the Section 4.4.1. Otherwise, we used the same permeability structure (realization A), water table depth at source location, and source strength (q_{CO2} = 1. x 10^{-4} kg s^{-1}). Figure 4.13 shows the initial liquid saturation field in the subsurface and the surface-layer winds for the 3 m s^{-1} case.

Shown in Figures 4.14 and 4.15 are results after 1, 10, and 200 years for the high CO_2 source strength of 1 x 10^{-4} kg s^{-1} and ambient winds of 3 m s^{-1} and 1 m s^{-1}. As shown, dilution in the atmospheric surface layer is very strong. Surface layer CO_2 concentrations due to seepage are of order 10^{-8} or smaller by mole fraction. This strong dilution occurs because the CO_2 mixes with ambient air very effectively by turbulence as modeled by variable-K theory.

As an aside, we note that relative to Figure 4.8a (permeability realization A, high source CO_2 flux, and 200-year simulation, tilted system), Figure 4.14c shows a greater extent of lateral

subsurface CO_2 flow. This difference can be attributed to the effects of the down-dip decreases in (1) vertical path length for CO_2 flow, and (2) size of the unsaturated zone (Figure 4.8a). In addition, the horizontal system of Figure 4.14c allows upward CO_2 flow only along vertical connections in the numerical grid, whereas the dipping system allows a vertical component of flow along both coordinate-axis directions.

4.5 Summary of Modeling Results

CO_2 migrates upward with little lateral diversion, even in a tilted heterogeneous permeability system. The travel time from approximately 100 m depth to the ground surface is approximately one year. The gas in the CO_2 plume is essentially pure CO_2 in the subsurface, even though the CO_2 flux is quite small. Surface-layer winds are capable of diluting CO_2 concentrations to very small values above the ground surface. These results have neglected lateral dispersion (transverse to wind velocity direction) and therefore somewhat overpredict actual surface-layer CO_2 concentrations. The high CO_2 concentrations observed in simulations at the ground surface and in the subsurface, relative to the atmospheric surface layer suggest that monitoring of CO_2 in the subsurface or at the ground surface may have greater potential to detect anomalous CO_2 of geothermal origin than above-ground techniques.

5. BACKGROUND CO_2 FLUXES AND CONCENTRATIONS

5.1 Introduction

We define "background" CO_2 as CO_2 derived mainly from the atmosphere and biologically mediated oxidation of organic carbon (respiration). We will not discuss CO_2 derived from leaking natural fossil hydrocarbon reservoirs here. Background soil CO_2 fluxes and concentrations are primarily dependent on three factors: (1) CO_2 production in the soil by biological processes, (2) flow of CO_2 from sub-soil sources into the soil column, and (3) exchange of CO_2 with the atmosphere by concentration and pressure-driven transport processes. Background soil CO_2 sources and exchanges are shown schematically in Figure 5.1 and are discussed in detail below.

5.2 CO_2 Production in Soil

Production of CO_2 in soils occurs primarily by root respiration and decay of organic matter (aerobic microbial respiration). The rate of root respiration is strongly dependent on the vitality of the plant (e.g., Mogensen, 1977). While litter and root exudates provide the source of carbon for decay processes, the decay rate and associated CO_2 production are largely dependent on soil temperature and moisture, substrate quality and availability, soil aeration, and pH (e.g., Wiant, 1967a; Wiant 1967b; Edwards, 1975; Singh and Gupta, 1977; Amundson et al., 1989; Wood et al., 1993). Both diurnal and seasonal temperature changes have been shown to strongly influence the rate of CO_2 production by root and microbial respiration processes, and related concentrations and fluxes; production in the soil generally increases with temperature (e.g., Parada et al., 1983; Amundson and Smith, 1988; Osozawa and Hasegawa, 1995). Soil water

content also strongly controls soil CO_2 production rate and it has been observed that between the permanent wilting point and 60–80% saturation, increasing water content increases the rates of soil CO_2 production (Alexander, 1977), whereas at higher or lower moisture contents, production rates can decrease (Kucera and Kirkham, 1971). Figure 5.2 shows repeated measurements of soil CO_2 concentration as a function of depth (hereafter referred to as CO_2 concentration profiles) at one site in central California. This time series of profiles demonstrates how soil CO_2 production and related concentrations can vary over time due to changes in soil temperature and water content (Lewicki et al., 2003a).

5.3 CO_2 from Sub-Soil Sources

Carbon dioxide may also enter soils from sources below at depth. Increasing CO_2 concentrations with depth down to the water table have been observed in a number of studies, indicating CO_2 production in the sub-soil (e.g., Wood and Petraitis, 1984; Keller, 1991; Keller and Bacon, 1998). This sub-soil production of CO_2 can occur by groundwater degassing of CO_2 that was originally derived from soil respiration or atmospheric sources and then dissolved in infiltration moving through the vadose zone. In addition, particulate organic carbon can be transported to depth by recharging groundwater and can be oxidized to CO_2 by microbes under aerobic conditions (e.g., Wood and Petraitis, 1984). Furthermore, if soil parent material contains ancient organic carbon and is exposed to aerobic conditions in the vadose zone, oxidation of this carbon will produce CO_2 (e.g., Keller and Bacon, 1998). CO_2 concentration profiles resulting from any of these processes will show increasing concentration with depth below the soil (e.g., Figure 5.3) and the CO_2 may then be transported upwards into the soil column.

5.4 Soil-Atmosphere Exchange of CO_2

Two main gas transport processes control exchange of soil CO_2 with the atmosphere, namely concentration-gradient-driven flow (diffusion) and total pressure-gradient-driven flow (advection). Diffusive flow is driven by the rate of gas production and the temperature, water content, porosity, and tortuosity of the soil. Advective transport can be driven by (1) atmospheric pressure effects whereby changes in atmospheric pressure can cause "pumping" of gas into and out of the soil (e.g., Massmann and Farrier, 1992), (2) temperature effects whereby changes in temperature may cause expansion or contraction of soil gas (e.g., Hinkle, 1994), (3) wind effects whereby changes in wind speed may promote gas flow through the soil (e.g., Reimer, 1980; Schery et al., 1984; Lewicki et al., 2003a), and (4) rainfall. Flow of rainwater through the soil can displace gas and "flush" CO_2 from the soil, leading to a temporary increase in soil CO_2 flux. Alternatively, precipitation may have a "capping" effect, slowing transport of CO_2 to the atmosphere and leading to rise of soil CO_2 concentrations (e.g., Hinkle, 1994).

6. METHODS FOR MONITORING CO_2

6.1 Introduction

A broad range of technologies is available to measure near-surface CO_2 concentrations and fluxes and determine the source of this CO_2 with the goal of detecting anomalous CO_2 of

geothermal origin. However, these techniques differ from one another in terms of the spatial and temporal scales of the measurement, measurement sensitivity and error, and cost. Overviews of CO_2 detection technologies can also be found in Shuler and Tang (2002) and Oldenburg et al. (2003).

6.2 Infrared Gas Analyzer

The infrared gas analyzer (IRGA) is an instrument commonly used to measure CO_2 concentration in subsurface or atmospheric air. The measurement is based on CO_2 absorption of infrared radiation within a gas sample cell. Portable IRGAs are available for use in the field and require only one person to operate. These IRGAs can be used to make single measurements or continuous measurements over time. Also, small IRGAs are available for installation in the subsurface or above ground and can be used for continuous monitoring of CO_2 concentration at fixed locations over time. Portable instrument set up and calibration usually require less than one hour and a single measurement can be made in seconds. The IRGA measurement range is variable; depending on the model and calibration, IRGAs are available to measure CO_2 concentration over a low range (e.g., 0-1000 ppmv CO_2) or over a high range (e.g., 0-100 vol% CO_2). The precision and accuracy of IRGAs can be as good as ± 0.2 ppmv at 350 ppmv (near atmospheric concentration) and ± 1%, respectively. The cost of equipment can be as low as about $500, but typically ranges from $5,000 to $30,000.

IRGAs are reliable instruments, reasonably priced, straightforward to use, and portable. As a result, IRGAs have been applied to a wide range of studies including occupational health and safety, ecosystem, volcanic/geothermal, micrometeorological, agricultural, and human physiology research. Although IRGAs make measurements of CO_2 concentrations at point locations, they can be coupled with additional instrumentation to measure surface CO_2 fluxes from small to large areas (see Accumulation Chamber and Eddy Covariance sections below). Additional information regarding commercially available IRGAs and their applications in research can be found in: Li-COR (2003); Oskarsson et al. (1999); Shuler and Tang (2002); Sorey et al. (1996); and USGS (2000a, 2000b).

6.2.2 Accumulation Chamber

The accumulation chamber (AC) method is used to measure soil CO_2 flux using an AC and an IRGA (Figure 6.1). Using this technique, an AC with an open bottom (cm^2 scale) is placed either directly on the soil surface or on a collar installed on the ground surface, the contained air is circulated through the AC and an IRGA, and the rate of change of CO_2 concentration in the chamber ($d[CO_2]/dt$) is measured by the IRGA and recorded. The flux of CO_2 (F) is then calculated according to

$$F = \left(\frac{\rho V}{A}\right)\left(\frac{d[CO_2]}{dt}\right) \tag{6.1}$$

where ρ is the molar density of air, V is the volume of the measurement system, and A is the area of the AC footprint. The accuracy and precision of the AC method have been estimated to be -

12.5 % (Evans et al., 2002) and ±10% (Chiodini et al., 1998), respectively. Each AC measurement typically is made within several minutes and one person is required to operate the instrumentation. The AC method has been applied in volcanic and geothermal studies where relatively high magnitude fluxes (up to 5 x 10^4 g m^{-2} d^{-1}) are present (e.g., Farrar et al., 1995; Chiodini et al., 2001; Salazar et al., 2001; Lewicki et al., 2003b), as well as in ecological studies (e.g., Rolston, 1986; Mosier, 1989; Norman et al., 1992, Gouldin et al., 1996) where relatively small magnitude CO_2 fluxes on the order of 40 g m^{-2} d^{-1} are typical.

Because the AC CO_2 flux measurement is regarded as a point measurement, many measurements are required to characterize the spatial variability of fluxes and to delineate spatial trends within a study area. To estimate the total CO_2 emissions from an area of interest, flux measurements are made at evenly spaced intervals along grids and the mean flux is multiplied by the surveyed area, or fluxes are measured at uneven spacing within the area, geostatistical methods are used to interpolate a flux grid, and volume and area integration algorithms are applied to this grid. It can be difficult with the AC method to evaluate the temporal variability of soil CO_2 fluxes that is typical for an area of interest and the influence of atmospheric parameters (temperature, pressure, wind, precipitation) on this variability. To characterize this temporal variability, researchers commonly install automated CO_2 flux measurement stations where single or multiple chambers measure flux repeatedly over time at point locations (e.g., Gouldin and Crill, 1997; Rogie et al., 2001; Lewicki et al., 2003a; Edwards and Riggs, 2003). The cost of the portable AC instrumentation typically ranges from $15,000 to $25,000.

6.2.3 Eddy Covariance

Eddy covariance (EC), or eddy correlation, is a technique whereby high frequency measurements of atmospheric CO_2 concentrations at a height (z) above the ground are made by an IRGA (Figure 6.2), along with measurements of micrometeorological variables such as wind velocity, relative humidity, and temperature. Integration of these measurements provides a gross conservation of energy and mass over an area of land (the EC footprint) from which the net CO_2 flux is derived. The equations and algorithms used to estimate the EC CO_2 flux are under constant development; however, the method essentially involves time-averaging the product of the time series of fluctuating CO_2 concentration ($c(x,y,z,t)$), and the time series of fluctuating vertical wind velocity ($w(x,y,z,t)$). Under steady-state conditions and for sufficiently long averaging time (typically 30 minutes to several hours), this converges to the ensemble mean flux, the average of the product of w and c. The measured vertical CO_2 flux is an integral of the surface flux over the upwind footprint. The size of this footprint (typically m^2 to km^2) scales with the measurement height and is also dependent on meteorological conditions during the time of measurement.

One advantage of EC is that it provides a spatially and temporally averaged measurement and therefore inherently filters out small-scale spatial and temporal variability in the surface flux, potentially providing a more representative measurement of the surface flux. Spatial and temporal averaging over large land areas also allows for more efficient measurement strategies. One limitation of the EC measurement is that it assumes a horizontal and homogeneous surface. Violations of this assumption include varying density of plant cover, land use, and topography and can introduce significant error into the measurement. In general, measurements should be

made over terrain with less than 8 to 15% slope (Baldocchi et al., 1988). Also, if surface heterogeneity occurs on a small scale and is randomly distributed or can be organized into regions of uniform surface conditions within which the EC measurement is made, measurement error can be reduced (e.g., Lenschow, 1995). Furthermore, the EC measurement should be made under statistically steady meteorologic conditions; morning and evening periods, as well as times of changing weather conditions should be avoided. Due to the significant error that can be introduced into the EC measurement from meteorological and terrain conditions at the study site, EC typically cannot provide temporally and spatially continuous measurements. Rather, gaps in time and space must be tolerated. Also, it is generally not possible to delineate spatial trends in surface CO_2 flux within the EC measurement footprint. A method such as AC must be used to accomplish this.

Typical ecological CO_2 fluxes in nature are 38 g m^{-2} d^{-1} efflux and 112 g m^{-2} d^{-1} uptake. The absolute range and minimum resolvable flux for EC have not been documented in the literature. Under favorable meteorologic and terrain conditions, the resolution of the EC method can be as good as 0.4 g m^{-2} d^{-1}. Estimates of the precision of EC vary from ± 5 to 30%. Short-term error has been estimated to be ± 7% during the daytime and ± 12% during the nighttime; long-term error is on the order of ± 5%. The capital cost for EC equipment typically ranges from $15,000 to $40,000, depending on tower size and meteorological instrumentation. The operating costs are primarily the power supply, labor, and time for a survey. EC has mainly been applied in meteorological, ecological, and terrestrial carbon cycle investigations, but has also been tested in volcanic environments. For detailed information on the theory of EC and its applications, readers are referred to Anderson and Farrar (2001), Baldocchi et al. (2001), Baldocchi and Wilson (2001), Foken and Wichura (1996), Gouldin et al. (1996), Li-Cor (2003), Massman and Lee (2002), and the USGS (2000a, b).

6.3 Hyperspectral Imaging

Hyperspectral imaging refers to the imaging of a region of interest over a large number of discrete, contiguous spectral bands, typically in the visible and near-IR. A complete reflectance spectrum is then derived for each pixel in the hyperspectral image. The reflectance spectra of most materials on the Earth's surface contain characteristic or diagnostic absorption features; these absorption features can therefore provide a means to identify surface materials. Hyperspectral data have been used in a wide range of studies, including mineral and geothermal exploration, vegetation mapping, hazardous material remediation, ecosystem monitoring, and agricultural problems. One important application of hyperspectral imaging to monitoring for CO_2 migration from hidden geothermal systems is the ability to detect changes in plant health and communities related to elevated soil CO_2 concentration (e.g., Martini et al., 2000).

The spectroradiometers used in hyperspectral imaging can be hand-held, truck-mounted, plane-mounted, or satellite-based and related survey areas vary from sub m^2 to greater than km^2. The material detection range depends on the signal to noise ratio of the acquired data and the strength of the material's spectral signature. Hyperspectral imaging can reconstruct net energy exchange, net primary production, or gross primary production with 20% error or less. Although individual measurements are rapid, the time required for data processing and analysis may range from days to weeks. However, high spatial resolution, high signal-to-noise, geo-rectified hyperspectral

data are currently available from commercial vendors. The cost of imaging an area of interest varies by orders of magnitude depending upon the platform for deployment. The main advantage of hyperspectral imaging to detection of hidden geothermal systems is the potential for remote sensing of CO_2 migration by proxy over large land areas. The main disadvantages are the potentially high cost of obtaining imagery and that the methodologies are still evolving. Further information on hyperspectral imaging, can be found the following websites: http://aviris.jpl.nasa.gov/ (JPL AVIRIS), www.earthsearch.com (Earth Search Sciences, Inc.).

6.4 Light Detection and Ranging

Light detection and ranging (LIDAR) can be used measure the concentrations of trace gases in the atmosphere (e.g., N_2O, SO_2, O_3, H_2O, CH_4, CO_2) with laser light. While there are a range of LIDAR techniques in use, atmospheric CO_2 concentration can be measured by differential absorption LIDAR (DIAL) or Raman LIDAR.

In the DIAL technique, a tunable laser is used at two wavelengths to estimate the concentration of a target-absorbing species. In the case of CO_2, one laser wavelength is selected to coincide with the center of a CO_2 absorption line and the second wavelength is selected to fall in a nearby non-absorbing region. Laser power at both wavelengths is transmitted over the same path in the atmosphere and is elastically scattered into the field of view of the LIDAR receiver. The average CO_2 concentration over the path length is then determined from the ratio of the backscatter signals for the two laser wavelengths.

In the Raman LIDAR method, laser light is transmitted into the atmosphere, the laser radiation is shifted in wavelength due to interaction with the target scattering molecules along the resolved path length, and this wavelength-shifted signal is detected by the LIDAR receiver. Raman scattering provides wavelength shifts that are unique to the target molecules, according to the vibrational energy states of the molecules. In the case of CO_2, the backscattered power of the wavelength-shifted signal is proportional to the average CO_2 concentration over the laser path length. By comparing the Raman signal of the CO_2 to the Raman signal of N_2 or O_2, CO_2 concentration can be quantified.

DIAL and Raman LIDAR can be deployed from a truck- or plane-based platform. Truck-based surveys can cover up to 10s of km^2 per day, whereas a given plane-mounted survey can potentially cover 10s to 100s of km^2. The detection range of DIAL and Raman LIDAR depends upon the wavelength and strength of absorption and typically ranges from <1 ppmv to several percent for CO_2. The precision for truck mounted or airborne measurements is generally from 1% to 5% of maximum range; from 3.4 to 27 ppmv at 1 km path length and from 14 to 86 ppmv at 2 km path length at 330 ppmv in clean air . The cost of DIAL and Raman LIDAR ranges from hundreds of dollars for a truck-mounted survey to thousands of dollars for an airborne survey. The advantages of Raman LIDAR and DIAL are that these are rapidly developing technologies with the potential to measure atmospheric CO_2 concentrations over multiple spatial scales, thus increasing the efficiency of the CO_2 survey. The main disadvantages are that they have the potential to be expensive and measure average concentration over a path length. Additional measurements are therefore required to locate the source(s) of CO_2 emissions along the path length. For a more detailed description of these methods, the reader is referred to Schlessinger (1995), Radziemski et al. (1987), Shuler and Tang (2002); Jet Propulsion Laboratory, National

Aeronautics and Space Administration, http://lidar.jpl.nasa.gov/, http://asd-www.larc.nasa.gov/lidar/lidar.html.

6.5 Long Open Path IR and Tunable Lasers

Measurement of atmospheric surface layer CO_2 concentration by long open path IR and tunable lasers occurs as a fixed laser sends pulses to one or more reflectors within a study area and the signal is returned to a detector at the beginning of the laser path. The infrared absorption is measured at CO_2-specific wavelengths and the cumulative CO_2 concentration over the laser path length is then determined. While still under development, a single instrument set-up has the potential to provide continuous monitoring of atmospheric surface layer CO_2 over several km^2. The detection range currently ranges from less than 1 ppmv to several percent CO_2 and measurement precision is expected to be ± 3% or better. Although these instruments are not yet developed to the point of commercial viability, the costs are projected to be thousands of dollars per unit. The primary advantage of long open path IR and tunable laser technology is the potential to monitor CO_2 concentration over a large area with automated, continuous measurement, and the main disadvantage is that it is still under development. Also, because it provides a measurement of cumulative CO_2 along the path length, additional point measurements are required to locate the source(s) of CO_2 along the path. For further description of long open path IR and tunable laser technology , see Shuler and Tang (2002) and Duarte (1995).

6.6 Micro-Electronic Mechanical Systems, Smart Dust, Motes

Micro-electronic mechanical systems (MEMS), Smart Dust, and Motes are miniaturized (mm^3 scale) sensing and communications platforms and are currently developing technologies. Applicable to CO_2 detection, is the incorporation of miniaturized infrared gas sensors into these platforms to measure absorption of IR radiation at CO_2-specific wavelengths. These technologies may therefore have the capability to measure CO_2 concentrations in the atmospheric surface layer and the subsurface. The promising aspect of these miniature devices is that numerous measurement systems could be distributed over a large study area to form a network that measures CO_2 concentrations and broadcasts the data to a single data recording location. Smart Dust is particularly attractive because it is small, inexpensively fabricated in mass quantities, could be easily scattered around a given area, and self-assembles into a network so that data collection and coverage are simplified. Since MEMS, Smart Dust, and Motes are currently under development; the sensitivity, precision, and time and length scales of the CO_2 concentration measurements are uncertain. The main disadvantage of these technologies is that they are currently under development. For more information on MEMS, Smart Dust, and Motes technologies, refer to http://www.ion-optics.com/.

7. STRATEGIES FOR DETECTION OF GEOTHERMAL CO_2

7.1 Introduction

As the previous section shows, a variety of technologies is available to measure CO_2 concentrations and fluxes in the subsurface and atmospheric surface layer, several of which are

rapidly developing and will extend our current capabilities and potentially lower the cost of CO_2 monitoring. However, successful application of these technologies to detect the signal of CO_2 from hidden geothermal systems within natural background variability is challenging when the geothermal CO_2 fluxes are very small. To meet the challenge of geothermal CO_2 detection, novel procedures and/or technologies may have to be developed. In this section, we present potential strategies based on currently available conventional technologies that could be applied toward the detection and quantification of geothermal CO_2.

7.2 Sub-Surface Gas Geochemistry

Relative to atmospheric gases, sub-surface gases are less prone to dilution of the geothermal CO_2 signal by background ecological and meteorological processes. As a result, monitoring for CO_2 migration from geothermal reservoirs should be focused on the subsurface. Both the carbon isotopic composition of CO_2 and bulk gas chemistry can be used to determine the origin of CO_2 and thereby potentially detect migration of CO_2 from a geothermal reservoir. For reference, Table 7.1 shows typical chemical and isotopic signatures related to CO_2 derived from different sources.

7.2.1 Bulk Chemical Composition of Soil Gas

The bulk chemical composition of gases collected at soil and sub-soil depths provides information on CO_2 production and the source of this CO_2 (i.e., whether it is derived from respiration or non-respiration sources). CO_2 concentration profiles measured with depth in the vadose zone can yield valuable information about CO_2 production. For example, an increase in CO_2 concentration with depth below the soil indicates CO_2 production at sub-soil depths. Production of CO_2 by oxidative decay of organic matter tends to consume O_2 at a similar rate. Also, atmospheric O_2 will diffuse down into the soil and sub-soil as sub-surface CO_2 diffuses to the atmosphere. A flux of geothermal CO_2 would produce elevated CO_2 concentration at depth, relative to the atmosphere, but would not be accompanied by O_2 consumption, although atmospheric O_2 would diffuse down into the soil. Based on these general processes, the CO_2 concentration and O_2 concentration profiles generated should be different, depending on whether a geothermal flux is present. Assuming that diffusion is the dominant gas transport process in the absence of a geothermal CO_2 flux, diffusion models could be used to predict the CO_2 concentration and O_2 concentration-depth profiles that result from expected background CO_2 respiration and O_2 consumption rates. One might expect groundwater degassing of respiration and atmospheric-derived CO_2 to show similar chemical trends within the vadose zone to degassing of geothermal CO_2. However, vadose zone CO_2 concentrations produced by groundwater degassing and biological respiration processes have generally been reported to be less than 13 vol.% CO_2 (e.g., Wood and Petraitis, 1984; Amundson and Davidson, 1990; Wood et al., 1993), whereas near-surface CO_2 concentrations associated with geothermal emissions could be much higher. For example, simulated geothermal source CO_2 fluxes of 57.6 to 576 g m^{-2} d^{-1} produce maximum near-surface CO_2 concentrations of ~10–80 vol.% ($1x10^5$ to $8x10^5$ ppmv, Figures 4.9, 4.11, and 4.12). Importantly, however, the maximum near-surface CO_2 concentration produced by a source CO_2 flux of 5.76 g $m^{-2}d^{-1}$ is only predicted to be ~2 vol.% ($2x10^4$ ppmv, Figures 4.9 and 4.10), which could be problematic to distinguish from background CO_2 concentrations. The spatial and temporal variability of background CO_2 concentrations typical of the ecosystem and geology of the study area should therefore be well characterized in

order to identify anomalously high CO_2 concentrations that may be related to migration of CO_2 from geothermal reservoirs.

7.2.2 Carbon Isotopes

Carbon isotopic compositions of CO_2 reflect the compositions and relative proportions of the contributing sources and therefore can serve as tracers of the origin of CO_2. Hereafter, carbon-13 values will be reported as $\delta^{13}C$, the deviation in parts per thousand (‰) of the $^{13}C/^{12}C$ ratio in the sample from that of the Pee Dee Belemnite (PDB) reference standard. Carbon-14 values will be reported as $\Delta^{14}C$, the deviation, in parts per thousand of the $^{14}C/^{12}C$ ratio in the sample from that of the reference standard (oxalic acid decay corrected to 1950). The stable carbon isotopic composition of CO_2 is measured by a lab-based mass spectrometer, whereas ^{14}C in CO_2 is measured by an accelerator mass spectrometer (AMS). Carbon isotopic analyses can occur following laboratory preparation of gases collected in the field using standard geochemical methods. The cost of $\delta^{13}C$ analysis typically ranges from $10 to $30 per sample, and $\Delta^{14}C$ analysis typically ranges from $200 to $600 per sample.

The background isotopic composition of CO_2 in the soil is typically affected by contributions of CO_2 from respiration (root and microbial) and the atmosphere. CO_2 in the present atmosphere has $\delta^{13}C$ and $\Delta^{14}C$ values close to -7 and 70‰, respectively. The $\delta^{13}C$ composition of CO_2 respired from plant roots is isotopically depleted relative to the atmosphere due to isotopic fractionation associated with photosynthesis and will have an isotopic composition similar to that of the plant. Likewise, the $\delta^{13}C$ composition of CO_2 derived from decay of soil organic material will be similar to the plant material. This composition will largely depend on the photosynthetic pathway (e.g., C_3 or C_4) of the plant. The bulk $\delta^{13}C$ compositions of C_3 plants (e.g., woody shrubs) range from –24 to –38 ‰, but are typically about –28‰ (O'Leary, 1988). C_4 plants (e.g., grasses that have evolved to conserve water) have $\delta^{13}C$ values from –6 to –19‰, but are typically near –14‰ (O'Leary, 1988).

The $\Delta^{14}C$ composition of soil-respired CO_2 is primarily affected by root-respired CO_2, CO_2 produced by decay of organic matter on time scales of less than one year, and CO_2 produced by decay of organic matter on several year to decadal time scales (e.g., Trumbore, 2000). CO_2 derived from the first two sources will have $\Delta^{14}C$ values similar to that of the present atmosphere, CO_2 derived from decay of organic matter on decadal time scales may be ^{14}C-enriched relative to the atmosphere due to the increase in ^{14}C in soil organic matter since nuclear weapons testing in the 1960's. With the exception of oxidation or warming of wetland or frozen soils, respectively, decay of ancient organic matter with depleted $\Delta^{14}C$ values contributes relatively little to the decomposition CO_2 flux in most soils (e.g., Trumbore, 2000). Seasonal variations in the $\Delta^{14}C$ values of soil-respired CO_2 have also been observed, with the highest values measured during the growing season (e.g., Keller and Bacon, 1998; Trumbore, 2000).

In most cases, respiration occurs predominantly in the soil zone (i.e., typically the upper one to two meters of the subsurface). For example, Keller and Bacon (1998) showed that in a Canadian pastureland, 98% of all subsurface respiration occurred in the soil. Therefore, the isotopic compositions of sub-soil CO_2 should be influenced by respiration to a significantly lesser degree than isotopic compositions of soil CO_2. However, CO_2 can be produced at lower rates at sub-soil

depths by various processes such as oxidation of organic matter. The $\delta^{13}C$ value of this CO_2 will be similar to the source material and may not vary significantly from those for soil-respired CO_2. Also, groundwater degassing of CO_2 derived from atmospheric and soil-respired sources can occur and the $\delta^{13}C$ value of this CO_2 will be controlled by the relative proportions of the CO_2 from these sources. The ^{14}C values of CO_2 produced by these sub-soil processes will depend on factors such as the age of the organic matter and the residence time of dissolved CO_2 in the groundwater. For example, oxidation of ancient organic matter (e.g., peat, kerogen) will produce CO_2 that is highly depleted or free of ^{14}C.

The $\delta^{13}C$ signature of CO_2 derived from geothermal sources (e.g., magmatic/metamorphic) typically ranges from -2 to -6‰ (Faure, 1986) and therefore will distinguish it from CO_2 derived from C_3, and many C_4 plants. However, it is similar to that of atmospheric CO_2 and therefore, when considered alone, will be problematic in distinguishing these sources. In addition, if groundwaters containing dissolved CO_2 of biologic origin circulate through areas of high heat flow and subsequently degas this CO_2, the $\delta^{13}C$ signature will be similar to the biologic source(s). Geothermal CO_2 derived from deep magmatic/metamorphic sources is ^{14}C-free. Leaking geothermal CO_2 will therefore have a ^{14}C signal that is distinct from atmospheric and most biogenic respiration sources. This signal should be easily distinguishable from dominant background CO_2 sources. For example, geothermal source CO_2 fluxes of 5.76, 57.6, and 576 g m^{-2} d^{-1} were described in Section 3. Given a background soil CO_2 respiration rate and $\Delta^{14}C$ composition typical of a temperate forest (i.e., 7.2 g $m^{-2}d^{-1}$ and 128 ‰, respectively (Trumbore, 2000)), by mass balance, the $\Delta^{14}C$ values of soil CO_2 samples will be -371, -874, and –986 ‰ for geothermal source fluxes of 5.76, 57.6, and 576 g m^{-2} d^{-1}, respectively. The differences between these values and the isotopic composition of background soil CO_2 are much greater than the precision of the ^{14}C analysis (e.g., ± 4–8 ‰ depending on the laboratory method used (Southon et al., 1993)); geothermal fluxes over this range of magnitudes would therefore be easily detectable by ^{14}C analyses of soil CO_2.

Production rates of CO_2 from background sub-soil sources should be significantly lower than those in the soil column (e.g., Wood and Patraitis, 1984; Keller and Bacon, 1998). Therefore, the range of geothermal fluxes of CO_2 discussed above should be readily detectable using carbon-13, and in the absence of a large source of CO_2 derived from respiration of ancient sedimentary organic carbon, carbon-14, isotopic analyses of CO_2 collected from sub-soil depths. Furthermore, if soil and sub-soil gas samples contain a contribution of CO_2 from a deep geothermal source, plots of $\delta^{13}C$ or $\Delta^{14}C$ of CO_2 versus CO_2 concentration can be examined for mixing trends between deep geothermal and shallow respiration derived CO_2. In other words, the chemical compositions of the soil and sub-soil gases should lie on a trend between gases with relatively low CO_2 concentration and high $\Delta^{14}C$ or low $\delta^{13}C$ (young biogenic-carbon dominated) and those with relatively high CO_2 concentration and low $\Delta^{14}C$ or high $\delta^{13}C$ (geothermal-carbon dominated). Figure 7.1 shows an idealized mixing trend between soil gases derived from these two end-member sources.

7.2.3 Measurement Strategies

Soil gas CO_2 concentrations can be measured at many locations within a large area using a soil probe and a portable IRGA. Using this method, a soil probe is driven down to the depth of interest (usually within the soil zone), gas is pumped from the soil to the IRGA by an internal

pump, and CO_2 concentration is measured, typically to ± 100 ppmv or 0.01%. Alternatively, a gas sample can be collected from the probe using a syringe and vial for chemical analysis by standard gas chromatographic methods. Each IRGA measurement or collection of a gas sample can be conducted within minutes, and as a result, many measurements can be made over relatively short periods of time within the measurement area. Importantly, CO_2 concentrations in the soil zone will be strongly influenced by background respiration processes, which could render detection of CO_2 concentration anomalies related to very small geothermal fluxes difficult. The spatial and temporal variability of background CO_2 concentrations should therefore be characterized in areas with similar climate, vegetation, and soil type to that being explored for geothermal CO_2 flow. Sampling of gases at sub-soil depths would be valuable to avoid large respiration signals. However, this sampling would require installation of numerous sampling wells to install permanent CO_2 concentration sensors or provide locations at which to collect gas samples for chemical analyses. Unless multiple sampling wells were previously in place throughout the study area, sub-soil gas sampling could be impractical.

Due to the time and cost involved in making numerous (e.g., hundreds to thousands) closely spaced measurements within a large measurement area, the researcher commonly makes fewer measurements at widely and unevenly spaced intervals. A range of geostatistical methods, for example, kriging (e.g., Isaaks and Srivatava, 1989) or sequential Gaussian simulation (Deutsch and Journel, 1998) can then be used to estimate CO_2 concentrations at unsampled locations within a grid. This grid can then be contoured to search for spatial trends in the data. Autocorrelation analysis of a spatial data set involves the calculation of correlation coefficients for the data as a function of separation distance between the measurements. Thus, contouring and autocorrelation analysis together can be used to look for spatial trends in the data that may be related to CO_2 migration from a hidden geothermal reservoir. For example, elevated CO_2 concentrations and a high degree of spatial autocorrelation of these concentrations along a linear trend may indicate CO_2 flow along a geologic structure and would require further (e.g., isotopic) evaluation of the origin of the CO_2.

7.3 Surface and Atmospheric CO_2 Concentrations and Fluxes

Seepage of CO_2 from a hidden geothermal reservoir may result in surface CO_2 fluxes and atmospheric surface layer CO_2 concentrations of high enough magnitude to detect within background variability of CO_2. The magnitude of these seepage CO_2 fluxes and atmospheric CO_2 concentrations will be determined by a range of factors such as the mode of CO_2 emission (e.g., focused versus diffuse flow) and atmospheric effects (e.g., wind and density-driven atmospheric dispersion).

Several methods are available to detect anomalous CO_2 concentrations related to geothermal seepage in the atmospheric surface layer. For example, fixed or portable IRGAs or fixed solid-state sensors could be used to measure CO_2 concentrations. Because these measurements would be made at point locations, numerous measurements over a potentially large study area would be required. In addition, due to the significant atmospheric dispersion and dilution of seeping CO_2 that is expected under normal wind speed conditions, anomalous CO_2 concentrations may only be a few 10's of ppmv above average ambient air (~370 ppmv) downwind from the source (Figure 3.13). The precision of fixed detectors (typically ± 1 ppmv or better) would allow the detection of these anomalous CO_2 concentrations; however, the cost of each detector would

likely preclude use of the many detectors required within a study area. The use of one or a few portable IRGAs would be much lower in cost. However, due to the precision of portable IRGAs (typically ±100 ppmv at best), it would not be possible to detect low anomalous CO_2 concentrations within background variability. Point measurements of CO_2 concentrations in the soil and sub-soil avoid several of the primary limitations of atmospheric CO_2 detection methods, and as a result, would likely be a preferred method to detect CO_2 migrating from geothermal sources.

One method available to detect anomalous soil CO_2 flux is the AC technique. Successful detection, however, will strongly depend on the magnitude of the geothermal source flux at depth. For example, for a simulated source flux of 576 g CO_2 m^{-2} d^{-1}, the maximum predicted surface CO_2 flux is about 30 to 100 g m^{-2} d^{-1} (Figures 4.9 and 4.12). This flux should be detectable within natural background variability of surface CO_2 fluxes using the AC method. However, in the case of moderate to low geothermal source fluxes of 57.6 and 5.76 g CO_2 m^{-2} d^{-1}, maximum predicted surface CO_2 fluxes are only about 10^{-4} to 10^{-1} (Figures 4.9-4.11), which would not be detectable using the AC method, given the measurement error.

Because the AC method essentially provides a "point" flux measurement (i.e., a measurement on the cm^2 scale), numerous measurements are required to characterize the spatial trends and variability of fluxes within a study area. However, the AC method offers the benefit over the EC method in that spatial trends in surface fluxes can be mapped, allowing for the location and geometry of potential areas of anomalously high CO_2 flux to be delineated, as described above for soil CO_2 concentrations. Also, the AC technique is generally more flexible than the EC method because it requires few terrain or atmospheric conditions to be met. Because the AC technique provides a point measurement in time and space (as opposed to the spatially and temporally averaged EC measurement), it can be difficult to evaluate the temporal variability of soil CO_2 fluxes that is typical for the study area and the influence of atmospheric parameters (temperature, pressure, wind, precipitation) on this variability. Therefore, automated CO_2 flux measurement stations must be deployed where single or multiple chambers measure flux repeatedly over time, along with meteorological parameters. The relationship between surface CO_2 flux and these meteorological parameters can then be evaluated using correlation analysis.

The EC method provides a spatially and temporally averaged surface CO_2 flux measurement that could be used to detect anomalous CO_2 emissions related to seepage of geothermal CO_2. To successfully detect anomalous CO_2 flux, however, EC instrumentation must be deployed under the meteorological and terrain conditions required to minimize the error of the measurement. Also, the magnitude of the CO_2 flux anomaly must be large enough such that it can be detected above background variability (which should be characterized for an ecosystem similar to that at the study site), given the error of the measurement. Additional point measurement (e.g., with the AC method) would also be required to delineate the location and geometry of the CO_2 flux anomaly within the EC footprint.

7.4 Water Chemistry

Geothermal CO_2 may also seep and dissolve into ground and surface waters. This CO_2 could be detected by ground and surface water sampling and chemical analysis. As CO_2 dissolves in

ground and surface waters, the acidity of the waters will tend to increase (i.e., the pH will decrease). A relatively large magnitude CO_2 seepage flux into ground or surface water could produce CO_2 gas bubbles and this CO_2 could be sampled for isotopic analyses ($\delta^{13}C$, $\Delta^{14}C$) to constrain its source, as described above for vadose zone CO_2. However, if seepage fluxes are small to moderate, CO_2 should be mainly present in the aqueous phase as dissolved inorganic carbon, DIC (i.e., $CO_2(aq)$, H_2CO_3, HCO_3^-, CO_3^{2-}). With increasing seepage of CO_2 into waters, DIC should increase. Alkalinity is the ability of water to accept protons (H^+) and is predominantly due to the presence of HCO_3^- and CO_3^{2-} in most potable natural waters. The DIC concentration can be directly determined or can be calculated if both alkalinity and pH are determined for a given water sample. Plots of DIC concentration versus $\Delta^{14}C$ or $\delta^{13}C$ of the DIC can then be used to trace the addition of deep magmatic/hydrothermal carbon to groundwaters that contain respiration-derived carbon from infiltration (e.g., Chiodini et al., 2000; Evans et al., 2002). The chemical trends in these waters indicate mixing between waters with relatively low DIC and high $\Delta^{14}C$ or low $\delta^{13}C$ (young biogenic-carbon dominated) and those with relatively high DIC and low $\Delta^{14}C$ or high $\delta^{13}C$ (magmatic/hydrothermal-carbon dominated). If the concentration of DIC derived from the deep source and water flow rate are known for sample locations within the study area, the discharge of deeply derived DIC can be estimated.

In order to successfully detect geothermal CO_2, a variety of factors must be considered in the interpretation of ground and surface water geochemistry. To evaluate the influence of residence time on the ^{14}C compositions of DIC, groundwater age should be assessed (e.g., by tritium analyses). Also, interactions between water and host rocks along flow paths can affect the concentration and isotopic composition of DIC, concentrations of major and minor cations in solution, and pH. For example, dissolution of calcium carbonate ($CaCO_3$) by the reaction $CO_2 + H_2O + CaCO_3 = Ca^{2+} + 2HCO_3^-$ results in the doubling of DIC (i.e., one mole of CO_2 reacts to produce two moles of HCO_3^-) and a release of Ca^{2+} to solution. Also, the DIC produced will have $\delta^{13}C$ and $\Delta^{14}C$ compositions reflecting contributions from both the CO_2 and the carbonate mineral. Therefore, the contribution of DIC derived from dissolution of ^{14}C-free and ^{13}C-enriched carbonate rocks along flow paths will decrease $\Delta^{14}C$ values and increase $\delta^{13}C$ values similarly to geothermal CO_2 and could complicate interpretation of DIC concentration-carbon isotopic composition plots.

Single or continuous aqueous geochemical measurements are usually made at fixed locations. These measurements can be made using portable field equipment (e.g., pH electrode, field alkalinity titration kit) or by analysis of water samples in a standard geochemical laboratory. Carbon isotopic compositions of water samples are determined as described above for soil gas samples. The detection range and precision are variable, depending on the measurement. Aqueous geochemical sampling and analytical techniques are well established, and relatively inexpensive (i.e., dollars to hundreds of dollars per sample). However, the spatial coverage of groundwater sampling is limited by the presence of wells or springs. Also, source water chemical composition, rock-water interactions along flow paths, and residence time can complicate interpretation of the groundwater geochemistry. In the case of surface waters, interpretations can be complicated by source water chemical composition, surface hydrology, and weather.

7.5 Statistical Analysis

7.5.1 Background

Statistical analysis can be used to refine sampling strategy and reduce the number of high-cost measurements made in the search for hidden geothermal systems. Assuming that the sampling method (e.g., IRGA for CO_2 concentration, AC method for soil CO_2 flux) has 100% capability to detect a gas anomaly, the probability (P) of sampling at least once a gas anomaly of area x at least once within a study area A with n number of randomly distributed point measurements is given by

$$P = 1 - \left[1 - \frac{x}{A}\right]^n \tag{7.2}$$

Therefore, if x/A = 0.1, ~30 measurements are required to sample a gas anomaly at least once with 95% confidence. If x/A = 0.01 and 0.001, ~300 and 3000 samples, respectively, are required to sample the anomaly at least once. Importantly, application of Eq. 7.2 assumes that a gas anomaly exists within area A. However, in the case we are particularly interested in, the researcher will search for a hidden geothermal system within an area where there is no evidence of surface hydrothermal features and there is likely a relatively low probability of the existence of a gas anomaly within this area. With Bayesian statistics, we are then able to answer the question: "Given that we have failed to detect (~d) a gas anomaly of area x within the sampling area A with one randomly located point measurement, what is the confidence level (P) that it is actually there (H)?" For this case,

$$P(H \mid \sim d) = \frac{\left(1 - \frac{x}{A}\right)P(H)}{P(H)\left[1 - \frac{x}{A}\right] + \left[1 - P(H)\right]} \tag{7.3}$$

(Bayes, 1763). To solve this equation, $P(H)$ is set equal to an initial confidence (e.g., 0.1 if the researcher is realistically pessimistic or 0.9 if realistically optimistic, that the anomaly is present within the study area), given some prior information about the study area. To estimate the number of randomly distributed point measurements (n) necessary for there to be, e.g., only a 5% chance that an anomaly exists, given that we have not detected it, the calculated $P(H \mid \sim d)$ is substituted for $P(H)$, the equation is solved iteratively until $P(H \mid \sim d)$ = 0.05, and n = the number of iterations. If the researcher strongly suspects that there is an anomaly within the study area, and $P(H)$ = 0.9, $n \approx$ 50, 500, 5000, and 50,000 for x/A = 0.1, 0.01, 0.001, and 0.0001, respectively. If $P(H)$ = 0.1, $n \approx$ 7, 70, 700, and 7000 for x/A = 0.1, 0.01, 0.001, and 0.0001, respectively.

Although any number of *x/A* scenarios may be possible, these examples demonstrate that in the case of preliminary gas sampling and analysis, rapid and economical methods should be used in order to accommodate a potentially large number of measurements. It is also necessary to collect site-specific geologic information prior to sampling to delineate the most probable locations of gas migration (e.g., near geologic structures) to minimize *A* and maximize *x/A*.

It is important to recognize that Eq. 7.3 assumes that the sampling methodology is 100% capable of detecting the gas anomaly. In other words, the detection method does not give false positives (i.e., it detects an anomaly that is not there) or negatives (i.e., it fails to detect an anomaly that is there). In reality, the methods used to detect a CO_2 anomaly within background CO_2 will likely give both false positives and negatives. In this case,

$$P(H \mid\sim d) = \frac{\left[(1-\frac{x}{A})(1-\alpha(m)) + \frac{x}{A}\beta(m)\right]P(H)}{\left[(1-\frac{x}{A})(1-\alpha(m)) + \frac{x}{A}\beta(m)\right]P(H) + \left[1-\alpha(m)\right]\left[1-P(H)\right]} \tag{7.4}$$

where $\alpha(m)$ and $\beta(m)$ are the false positive and negative rates, respectively, as a function of the magnitude (m) of the anomaly. The confidence that once an anomaly has been detected it is a true anomaly ($P(H \mid \sim d)$, given $\alpha(m)$ and $\beta(m)$ of the detection method, is then given by

$$P(H \mid d) = \frac{\left[\frac{x}{A}(1-\beta(m)) + (1-\frac{x}{A})\alpha(m)\right]P(H)}{\left[\frac{x}{A}(1-\beta(m)) + (1-\frac{x}{A})\alpha(m)\right]P(H) + \alpha(m)\left[1-P(H)\right]} \tag{7.5}$$

In order to apply Eqs. 7.4 and 7.5, $\alpha(m)$ and $\beta(m)$ must be estimated. For a given measurement method, for example, soil CO_2 flux measurement by AC, $\alpha(m)$ and $\beta(m)$ are related to the probability density functions (PDFs) of the background and anomalous CO_2 fluxes, respectively, and the chosen threshold above which CO_2 flux is considered anomalous. In other words, $\alpha(m)$ is the fraction of the background PDF that lies above the threshold value and $\beta(m)$ is the fraction of the anomaly PDF that lies below the threshold value. The PDFs of the background and anomalous CO_2 flux can be estimated from background field characterization and numerical modeling of geothermal CO_2 flow ± laboratory experiments, respectively. The threshold value is then found where the influence of $\alpha(m)$ and $\beta(m)$ on n is minimized. Monte Carlo simulation taking $P(H)$, x/A, $\alpha(m)$, and $\beta(m)$ into account can be used to estimate the number of measurements that will be required to determine with a desired confidence level that a gas anomaly exists in the sampling area (see Examples section below). In the field, the researcher would apply Eqs. 7.4 and 7.5 by beginning with an initial confidence that a geothermal anomaly exists within study area *A*. Measurements would be made within this area and Eqs. 7.4 or 7.5 would be solved repeatedly, depending on whether an anomaly is not detected or detected,

respectively. If the number of measurements that do not detect an anomaly increases, then the confidence that an anomaly exists decreases (Eq. 7.4). Conversely, if the number of measurements that detect an anomaly increases, then so does the confidence that the anomaly exists (Eq. 7.5). Measurements could be made until the desired confidence level is met that an anomaly exists in the sampling area.

Eqs. 7.4 and 7.5 have the potential to guide sampling strategy and reduce the number of high-cost (e.g., isotopic) measurements made. For example, when measured CO_2 fluxes and/or concentrations have been determined with high confidence to be anomalous, these sites can then be further sampled for isotopic analyses to determine if the CO_2 source is geothermal. Or, if a sufficiently low confidence level that an anomaly exists is reached, then further geochemical analyses can be avoided. While we describe the application of Eqs. 7.2–5 in the context of randomly distributed measurements, these equations can also be applied if measurements are made at evenly spaced intervals along a grid. However, if measurements are spatially clustered, Eqs. 7.2–5 cannot be used.

7.5.2 Examples

Introduction. In this section, we describe several cases where we use the PDFs of a background soil CO_2 flux data set measured by the AC method in central California (Lewicki et al., 2003a) and of anomalous geothermal CO_2 flux estimated based on numerical modeling (see Section 4, above) to estimate the *n* required to determine with a confidence level of 99% that a gas anomaly exists within a hypothetical sampling area. This hypothetical sampling area is assumed to have vegetation type and sub-surface physical properties similar to that at the background central California site, so that the measured soil CO_2 fluxes can be considered typical of background fluxes at the hypothetical site.

In each of the cases explored, we use Monte Carlo simulations to determine the threshold CO_2 flux where the influence of $\alpha(m)$ and $\beta(m)$ on *n* is minimized, and therefore, the minimum *n* required to detect a CO_2 anomaly with a confidence level of 99%. First, $\alpha(m)$ and $\beta(m)$ are calculated based on the background and anomaly PDFs, respectively, for threshold values from 1 to 50 g m^{-2} d^{-1}. Then, for each of the $\alpha(m)$-$\beta(m)$ value sets associated with each of the 50 threshold values and assuming given *x/A* and *P(H)* values, 500 Monte Carlo simulations are conducted. Each of these Monte Carlo simulations estimates *n* by random sampling of an initial CO_2 flux value and iteratively solving Eqs. 7.4 and 7.5 until a confidence level of 99% is met that the CO_2 anomaly exists. Because cases where extreme numbers of samples are needed to detect an anomaly are unrealistic based on the time and cost required for the sampling, a cutoff of $n = 20{,}001$ is assigned. Based on the 500 simulations, a PDF of *n* is constructed for each threshold value. The PDFs for all threshold values are compiled in an image plot (i.e., probability density as a function of threshold value and *n*) and used to determine the minimum *n* required to detect the CO_2 anomaly, and its associated threshold value. To explore the influences of (1) near-surface permeability structure, (2) *P(H)*, and (3) *x/A* on *n*, we vary each of these parameters individually, while holding the remaining parameters constant in the Monte Carlo simulations for Cases 1-12 (Table 7.2). Also, we only consider the high modeled geothermal source CO_2 flux because the surface fluxes associated with the low and medium source fluxes are below the detection limits of the AC method, as discussed above.

Homogeneous and isotropic permeability. Figure 7.2a shows the PDFs of measured background soil CO_2 flux (Lewicki et al., 2003a) and modeled anomalous surface CO_2 flux associated with homogeneous and isotropic permeability structure and high source CO_2 flux (see Figure 4.9 for the anomalous CO_2 flux profile). Based on these PDFs, $\alpha(m)$ and $\beta(m)$ were calculated for threshold values from 1 to 50 g $m^{-2}d^{-1}$. Holding $P(H)$ = 0.1 (indicating realistic pessimism that an anomaly exists), x/A was varied from 0.1 to 0.001 (Cases 1-3, Table 7.2) for Monte Carlo simulations. Then, x/A was varied from 0.1 to 0.001, holding $P(H)$ = 0.9 (Cases 4-6, Table 7.2), indicating realistic optimism that an anomaly exists. Figure 7.3 shows PDF image plots for Cases 1 and 2. For a given threshold value on these plots, high probability indicates that the n is appropriate to detect a CO_2 anomaly with 99% confidence. Also, the goal here is to determine the minimum n required to detect an anomaly. Therefore, we are specifically interested to find the location on the plot where probability is maximized and n is minimized.

On the Case 1 plot corresponding to $P(H)$ = 0.1 and x/A = 0.1 (Figure 7.3), high probabilities corresponding to minimum n values are evident at threshold values < 8 g m^{-2} d^{-1} and ~28 g m^{-2} d^{-1}. These threshold values approximately correspond to the "cross-over" points between the background and anomaly PDFs (Figure 7.2a). In other words, relative to measured background CO_2 flux, there is a high probability of occurrence of anomalous CO_2 flux at < 8 and ~30 g $m^{-2}d^{-1}$, while there is a relatively high probability of occurrence of background CO_2 flux at intermediate values. However, because (1) the low anomalous CO_2 fluxes would not likely be detectable using the AC method, and (2) the measured background soil CO_2 flux data set may not accurately represent the occurrence of low CO_2 flux values at the study site, the portion of the probability image plots at threshold values < 8 g $m^{-2}d^{-1}$ will hereafter be ignored. The threshold value of 26 g m^{-2} d^{-1} therefore likely represents the value where the influence of $\alpha(m)$ and $\beta(m)$ on n is minimized for Case 1. The mean (μ) and standard deviation (σ) of n at a threshold value = 28 g m^{-2} d^{-1} are shown on Table 7.3. The mean (μ) and σ are taken to be the minimum number of measurements required to detect a CO_2 anomaly within the sampling area and its uncertainty, respectively. For Case 1, n = 5415 ± 3029 (Table 7.3).

Also shown on Figure 7.2 is the Case 2 (x/A = 0.01) probability image plot. This plot indicates that >20,000 samples are required to detect an anomaly associated with x/A = 0.01. For x/A = 0.001 (Case 3), >20,000 samples are also required to detect an anomaly. Figure 7.4 shows probability image plots for Cases 4 and 5, where $P(H)$ = 0.9 and x/A = 0.1 and 0.01, respectively. For Case 4, n = 1869 ± 1784 (threshold = 29 g m^{-2} d^{-1}) and for Case 5 n = 19,984 ± 256 (threshold = 28 g m^{-2} d^{-1}) (Table 7.3). For Case 6 (x/A = 0.001), n > 20,000. Increasing the initial confidence level that an anomaly exists in the study area therefore leads to a decrease in n.

Heterogeneous and isotropic permeability. Figure 7.2b shows the PDFs of background central California soil CO_2 flux (Lewicki et al., 2003a) and anomalous CO_2 flux associated with the heterogeneous and isotropic permeability realizations A-E and high source CO_2 flux (see Figure 4.12 for the anomalous CO_2 flux profiles that were combined to produce the anomalous PDF). Based on these PDFs, $\alpha(m)$ and $\beta(m)$ were calculated for threshold values from 1 to 50 g m^{-2} d^{-1}. Holding $P(H)$ = 0.1, x/A was varied from 0.1 to 0.001 (Cases 7-9, Table 7.2) for Monte Carlo simulations. Then, x/A was varied from 0.1 to 0.001, holding $P(H)$ = 0.9 (Cases 10-12, Table 7.2). Figure 7.5 shows probability image plots for Cases 7 and 10. For Case 7 (x/A = 0.1), n = 3407 ± 1919 for a threshold value of 38 g m^{-2} d^{-1}. Relative to the Case 1 simulations for homogeneous permeability, fewer samples are required for detection of a CO_2 anomaly

associated with heterogeneous permeability. This can be attributed to the greater occurrence probability of high (i.e., >38 g m^{-2} d^{-1}) anomalous CO_2 fluxes associated with the heterogeneous subsurface permeability (Figure 7.2b), relative to homogeneous permeability (Figure 7.2a). For Cases 8 and 9 (x/A = 0.01 and 0.001, respectively), >20,000 samples are required to detect a CO_2 anomaly. When $P(H)$ = 0.9, n decreases; n = 1267 ± 1253 for a threshold value of 38 g m^{-2} d^{-1} and x/A = 0.1 (Case 10, Figure 7.4). Decreasing x/A to 0.01 and 0.001, results in n = 19,984 ± 256 (Case 11, Figure 7.6) and >20,000, respectively.

It is likely that "real-world" study areas will be characterized by heterogeneous permeability structure. As a result, fewer samples will likely be required, relative to the simulated cases with homogeneous permeability, with all else being equal (i.e., x/A, geothermal source CO_2 flux, $P(H)$). Overall, however, all Monte Carlo simulations demonstrate that, even for anomalous surface CO_2 fluxes associated with the high source CO_2 flux and heterogeneous permeability, a large number of measurements are required to detect anomalous flux with high confidence. It therefore will become critical to limit A in order to maximize x/A and reduce the number of required samples by detailed site characterization (e.g., by identification of structural features likely to provide high permeability pathways for gas transport and limitation of study area A to these features).

7.6 Integrated Sampling Strategy

The selection of a study area targeted for geothermal exploration will depend on a variety of geologic, geographic, and ecological factors. For example, the site may be located adjacent to a known geothermal resource. Or, the site may be selected because it possesses similar geologic and tectonic features to a known geothermal resource. Furthermore, recent vegetation kill potentially related to elevated soil-CO_2 concentrations may provide the impetus to conduct a survey to search for geothermal CO_2.

Importantly, the natural spatial and temporal variability of near-surface CO_2 should also be characterized in a background area with similar geologic, climatic, and ecosystem characteristics to the area targeted for geothermal exploration. To evaluate the overall spatial distribution of soil CO_2 fluxes and concentrations within the background area, these parameters should be measured using the AC method and a portable IRGA within the area along a large grid at widely spaced sampling intervals. Also, to understand the small-scale spatial heterogeneity of soil CO_2 fluxes and concentrations, measurements should be made along a smaller grid at closely spaced sampling intervals. To capture diurnal and seasonal variations in CO_2, measurements of soil CO_2 concentration, flux, and isotopic composition should be made repeatedly over time at several fixed "representative" sites. If feasible, atmospheric temperature, pressure, and wind speed and direction should be measured at a weather station contemporaneously with AC CO_2 fluxes. Soil temperature and moisture should also be monitored concurrently with soil CO_2 fluxes. Correlation analysis of soil CO_2 flux and environmental parameters should be performed. Using regression analysis, empirical relationships between correlated parameters could be established and used to predict the background CO_2 fluxes expected under a given set of environmental conditions. If the background study area meets the terrain conditions required by the EC method, then an EC station should be deployed during times of optimal meteorological conditions to measure spatially averaged net CO_2 fluxes.

A broad range of measurements should be made within the area targeted for geothermal exploration. However, as demonstrated by our modeling results, elevated sub-soil and soil CO_2 concentrations are expected to be the strongest and most easily detected signals related to CO_2 migration away from a hidden geothermal reservoir. As a result, initial sampling priority should be given to the measurement of these concentrations. In particular, the collection of sub-soil gas and water samples from wells for geochemical analyses promises a relatively high potential to detect leaking geothermal CO_2. Therefore, if previously installed wells exist within the study area, these wells should be sampled for analysis. However, because there is likely to be a relatively low density of pre-existing wells within the study area, a strong emphasis should also be put on rapid, economical, low-error measurements of soil CO_2 concentration and surface CO_2 fluxes along grids at evenly spaced intervals. These measurements should be focused during seasonal times of low ecological productivity to minimize biological respiration and maximize potential deep geothermal contribution of CO_2.

The two primary goals of soil CO_2 concentration and flux sampling are to minimize the number of these measurements (n), and to locate "high-probability" anomalies (Eqs. 7.4 and 7.5) where more costly deep sampling and isotopic measurements will then be conducted. To accomplish these goals, x/A (Eqs. 7.4 and 7.5, in the case where measurement methods are not 100% capable of detecting anomalous CO_2) should be maximized by focusing soil CO_2 concentration and AC CO_2 flux sampling in areas where geothermal CO_2 migration is most likely (e.g., near geologic structures). Secondly, the probability distributions of the background and anomalous soil CO_2 concentration (or flux) should be estimated from background field characterization and numerical modeling of geothermal CO_2 migration, respectively, and threshold values should be defined above which these parameters are considered anomalous. These CO_2 concentration and flux threshold values are chosen based on minimization of $\alpha(m)$ and $\beta(m)$ and therefore n (Eqs. 7.4 and 7.5). Equations 7.4 and 7.5 should then be used to determine the presence (or absence) of CO_2 anomalies with high confidence. The information provided on the locations of high-probability gas anomalies should be integrated with maps contoured for soil CO_2 concentration and flux magnitude and autocorrelation and cross-correlation coefficients of these parameters. Based on these combined analyses, the locations of more costly and time-intensive sampling can be determined.

Where anomalously high soil CO_2 concentration and flux are located, new wells should be installed and gases should be sampled at regular intervals from the surface to the water table for chemical and isotopic compositions. A source of CO_2 at depth would be accompanied by an increase in CO_2 concentration with depth. To check for a biological respiration source of CO_2 at (sub-soil) depth, measured CO_2 and O_2 concentration-depth profiles should be compared to profiles generated by diffusion models of background CO_2 respiration and O_2 consumption. Profiles of $\delta^{13}C$ and $\Delta^{14}C$ should be measured. Relatively low $\Delta^{14}C$ and high $\delta^{13}C$ values would be expected at depth with a leaking geothermal CO_2 source and mass balance calculations could be used to estimate the fraction contribution of this component to sampled CO_2. In sum, the observations of CO_2 and O_2 concentration gradients, CO_2 production distribution, surface CO_2 fluxes, and carbon isotopic compositions must be consistent with the CO_2 source.

If the terrain conditions in the study area are such that the errors of EC measurements are low enough to detect potentially small geothermal seepage fluxes, EC could be used as an additional tool to search for CO_2 seepage. Then, if the measured EC flux is sufficiently higher than the flux

variability measured at the background site to be considered anomalous, AC and soil CO_2 concentration measurements should be used detect the location and geometry of the anomaly within the EC footprint. To minimize *x/A* and the number of necessary AC and CO_2 concentration measurements, the EC instrumentation (e.g., tower height) should be configured to yield small footprint areas.

8. CONCLUSIONS

The properties of CO_2 and the methods for detection and monitoring of CO_2 are generally well known. We are also able to obtain a better understanding of near-surface CO_2 concentrations and fluxes resulting from CO_2 migration and seepage from hidden geothermal reservoirs using numerical simulation of CO_2 flow and transport. Yet despite this understanding, detecting small anomalous geothermal CO_2 fluxes and concentrations within natural background variations of CO_2 poses a challenge. The strategy that we propose involves integrated monitoring, modeling, and statistical analysis to understand the natural system. Once this understanding is achieved, integrated measurement, monitoring, and sampling technologies can be applied toward the characterization of CO_2 within the area potentially hosting a hidden geothermal reservoir. If measurements of CO_2 concentrations and fluxes within this area are suggestive of the presence of CO_2 derived from a geothermal source, the area should be investigated further by more cost- and time-intensive vertical profile sampling and isotopic analyses. Integrated analysis of all measurements will determine definitively if CO_2 derived from a deep geothermal source is present, and if so, the spatial extent of the anomaly. The appropriateness of further geophysical measurements, installation of deep wells, and geochemical analyses of deep fluids can then be decided based on the results of the near surface CO_2 monitoring program.

ACKNOWLEDGMENTS

We thank Pat Dobson and Mark Conrad (LBNL) for constructive comments and thorough reviews of this report. This work was supported by the Assistant Secretary for Energy Efficiency and Renewable Energy, Office of Geothermal Technologies, of the U.S. Department of Energy, and by the Office of Science, U.S. Department of Energy, under Contract No. DE-AC03-76SF00098.

REFERENCES

Alexander, M., Introduction to Soil Microbiology, 2nd ed., John Wiley and Sons, New York, 467 pp., 1977.

Amundson, R.G. and V.S. Smith, Annual cycles of physical and biological properties in an uncultivated and irrigated soil in the San Joaquin Valley of California, *Agriculture, Ecosystems, Env., 20*, 195–208, 1988.

Amundson, R.G., O.A. Chadwick, and J.M. Sowers, A comparison of soil climate and biological activity along an elevation gradient in the eastern Mojave Desert, *Oecologia, 80*, 395–400, 1989.

Amundson, R.G. and E.A. Davidson, Carbon and nitrogeneous gases in the soil atmosphere, *J. Geochem. Explor*., 38, 13-41, 1990.

Anderson, D.E. and C.D. Farrar, Eddy covariance measurement of CO_2 flux to the atmosphere from an area of high volcanogenic emissions, Mammoth Mountain, California, *Chem. Geology, 177*, 31-42, 2001.

Arya, S.P., *Air Pollution Meteorology and Dispersion*, Oxford University Press, 1999.

Baldocchi, D.D., Hicks, B.B. and Meyers, T.P., Measuring biosphere-atmosphere exchanges of biologically related gases with micrometeorological methods, *Ecology, 69*, 1331–1340, 1988.

Baldocchi, D.D. and K.B. Wilson, Modeling CO_2 and water vapor exchange of a temperate broadleaved forest across hourly to decadal time scales, *Ecological Modelling*, *142*, 155–184, 2001.

Baldocchi, D.D, E. Falge, L., Gu, , R. Olson, D. Hollinger, S. Running, P. Anthoni, Ch. Bernhofer, K. Davis, J. Fuentes, A. Goldstein, G. Katul, B. Law, X. Lee, Y. Malhi, T. Meyers, J.W. Munger, W. Oechel, K. Pilegaard, H.P. Schmid, R. Valentini, S. Verma, T. Vesala, K. Wilson and S. Wofsy, 2001, FLUXNET: A New Tool to Study the Temporal and Spatial Variability of Ecosystem-Scale Carbon Dioxide, Water Vapor and Energy Flux Densities, *Bull. Am. Meteorol. Soc., 82*, 2415-2435, 2001.

Bayes, T., An essay towards solving a problem in the doctrine of Chances, *Philosophical Transactions of the Royal Society of London, 53*, 370–418, 1763.

Benoit, D., Conceptual models of the Dixie Valley, Nevada Geothermal Field, *Geoth. Resour. Council Trans., 23,* 505-511, 1999.

Bergfeld, D., F. Goff, and C.J. Janik, Elevated carbon dioxide flux at the Dixie Valley geothermal field, Nevada; relations between surface phenomena and the geothermal reservoir, *Chem. Geol., 177*, 43-66, 2001.

Britter, R.E., Atmospheric dispersion of dense gases, *Ann. Rev. Fluid Mech.*, *21*, 317–344, 1989.

Cardellini, C., G. Chiodini, F. Frondini, D. Granieri, J. Lewicki, and L. Peruzzi, Accumulation

chamber measurements of methane fluxes: application to volcanic-geothermal areas and landfills, *Appl. Geochem., 18*, 45-54, 2003.

Chiodini, G., G. R. Cioni, M. Guidi, B. Raco, and L. Marini, Soil CO_2 flux measurements in volcanic and geothermal areas, *Appl. Geochem., 13*, 543–552, 1998.

Chiodini, G., F. Frondini, C. Cardellini, F. Parello, and L. Peruzzi, Rate of diffuse carbon dioxide earth degassing from carbon balance of regional aquifers: The case of the central Apennine, Italy, *J. Geophys. Res., 105*, 8423-8434, 2000.

Chiodini, G., C. Cardellini, F. Frondini, D. Granieri, L. Marini, and G. Ventura, CO_2 degassing and energy release at Solfatara Volcano, Campi Flegrei, Italy, *J. Geophys. Res., 106*, 16,213–16,221, 2001.

Cruz, J.V., R.M. Couthinho, M.R. Carvalho, N. Oskarrson, and S.R. Gislason, Chemistry of waters from furnas volcano, Sao Miguel, Azores: fluxes of volcanic carbon dioxide and leached materials, *J. Volcanol. Geotherm. Res., 92*, 151-167, 1999.

Deutsch, C.V. and A.G. Journel, *GSLIB, Geostatistical Software User's Guide*, Oxford Univ. Press, New York, NY, 1998.

Duarte, F.J., Tunable Laser Applications, *Optical Engineering Series No.50*, Marcek Dekker, Inc., New York, NY, 1995.

Edwards, N.T., Effects of temperature and moisture on carbon dioxide evolution in a mixed deciduous forest floor, *Soil Sci. Soc. Am. Proc., 39*, 361–365, 1975.

Edwards, N.T. and B.M. Ross-Todd, Soil carbon dynamics in a mixed deciduous forest following clear-cutting with and without residual removal, *Soil Sci. Soc. Am. J., 47*, 1014–1021, 1983.

Edwards, N.T. and J.S. Riggs, Automated monitoring of soil respiration: a moving chamber design, *Soil Sci. Soc. Am. J., 67*, 1266-1271, 2003.

Ellis, A.J. and W.A.J. Mahon, *Chemistry and Geothermal Systems*, Academic Press, New York, 1977.

Evans, W. C., M. L. Sorey, A. C. Cook, B. M. Kennedy, D. L. Shuster, E. M. Colvard, L. D. Wjite, and M. L. Huebner, Tracing and quantifying magmatic carbon discharge in cold groundwaters: lessons learned from Mammoth Mountain, USA, *J. Volcanol. Geother, Res., 114*, 291–312, 2002.

Farrar, C. D., M. L. Sorey, W. C. Evans, J. F. Howle, B. D. Kerr, B. M. Kennedy, Y. King, and J. R. Southon, Forest-killing diffuse CO_2 emission at Mammoth Mountain as a sign of magmatic unrest, *Nature, 376*, 675–678, 1995.

Faure, G., *Principles of Isotope Geochemistry*, John Wiley and Sons, New York, NY, 1986.

Favara, R. S. Giammanco, S. Inguaggiatio, G. Pecoraino, Preliminary estimate of CO_2 output from Pantelleria Island volcano (Sicily, Italy): evidence of active mantle degassing, *Appl. Geochem., 16,* 883-894, 2001.

Foken, Th. and B. Wichura, Tools for quality assessment of surface-based flux measurements, *Agric. For. Meteorol., 78*, 83-105, 1996.

Gerlach, T.M., M.P. Doukas, K.A. McGee, and R. Kessler, Soil efflux and total emission rates of magmatic CO_2 at the Horseshoe Lake tree kill, Mammoth Mountain, California, *Chem Geol., 177*, 101-116, 2001.

Gouldin, M.L., J.W. Munger, S.-M. Fan, B.C. Daube, and S.C. Wofsy, Measurements of carbon sequestration by long-term eddy covariance: methods and a critical evaluation of accuracy, *Global Change Biology, 2*, 169–182, 1996.

Gouldin, M.L. and P.M. Crill, Automated measurements of CO_2 exchange at the moss surface of a black spruce forest, *Tree Physiology, 17*, 537-542, 1997.

Hernandez, P.A., J.M. Salazar, Y. Shimoike, T. Mori, K. Notsu, and N. Perez, Diffuse emission of CO_2 from Miyakejima volcano, Japan, *Chem. Geol., 177*, 175-185, 2001.

Hinkle, M.E., Environmental conditions affecting concentrations of He, CO_2, O_2, and N_2 in soil gases, *Appl. Geochem., 9*, 53–63, 1994.

Isaaks, E.H. and R.M. Srivastava, *An Introduction to Applied Geostatistics*, Oxford University Press, New York, NY, 1989.

Keller, C.K., Hydrogeochemistry of a clayey till, 2, Sources of CO_2, *Water Resour. Res., 27*, 2555–2564, 1991.

Keller, C.K. and D.H. Bacon, Soil respiration and georespiration distinguished by transport analyses of vadose CO_2, $^{13}CO_2$, and $^{14}CO_2$, *Global Biogeochem. Cycles, 12*, 361–372, 1998.

Klusman, R.W., J.N. Moore, and M.P. LeRoy, Potential for surface gas flux measurements in exploration and surface evaluation of geothermal resources, *Geothermics*, *29*, 637-670, 2000.

Koepenick, K.W., S.L. Brantley, J.M. Thompson, G.L. Rowe, A.A. Nyblade, and C. Moshy, Volatile emissions from the crater and flank of Oldoinyo Lengai volcano, Tanzania, *J. Geophys. Res., 101*, 13,819-13,830, 1996.

Kucera, C.L. and D.L. Kirkham, Soil respiration studies in tallgrass prairie in Missouri, *Ecology, 52*, 912–915, 1971.

Lenschow, D.L., Micrometeorological techniques for measuring biosphere-atmosphere trace gas

exchange. In *Biogenic Trace Gases: Measuring Emissions from Soil and Water* edited by P.A. Matson and R.C. Harriss, Blackwell Science, Cambridge, 126–163, 1995.

Lewicki, J.L., W.C. Evans, G.E. Hilley, M.L. Sorey, J.D. Rogie, and S.L. Brantley, Shallow soil CO_2 flow along the San Andreas and Calaveras faults, California, *J. Geophys. Res., 108*, ECV 3-1 – ECV 3-14, 2003a.

Lewicki, J.L., C. Connor, K. St-Amand, J. Stix, and W. Spinner, Self-potential, soil CO_2 flux, and temperature on Masaya volcano, Nicaragua, *Geophys. Res. Lett., 30*, 1817, 2003b.

LI-COR Product Information Brochure, 2003. http://env.licor.com.

Magee, J.W., J.A. Howley, and J.F. Ely, A predictive model for the thermophysical properties of carbon dioxide rich mixtures, *Research Report RR-136*, Gas Processors Assoc., Tulsa OK, 35 pp., 1994.

Martini, B.A., D.C. Potts, E.A. Silver, and W.L. Pickles, Hyperspectral Remote Sensing for Research and Monitoring in Active Volcanic Regions: Long Valley Caldera, CA. *EOS Trans. Am. Geophys. Union*, Fall Meeting p. F1385, 2000.

Massmann, J., and D. Farrier, Effects of atmospheric pressures on gas transport in the vadose zone, *Water Resour. Res., 28*, 777–791, 1992.

Massmann, W.J. and X. Lee, Eddy covariance flux corrections and uncertainties in long term studies of carbon and energy exchanges, *Agric-For-Meteorol., 113*, 121-144, 2002.

McKenna, J.R., and D.D. Blackwell, Numerical modeling of transient Basin and Range extensional geothermal systems, *Geothermics*, *33*, 457-476, 2004.

Mogensen, V.O., Field measurements of dark respiration rates of roots and aerial parts in Italian ryegrass and barley, *J. Appl. Ecol., 14*, 243–252, 1977.

Mosier, A.R., Chamber and isotope techniques, in *Exchange of trace gases between ecosystems and the atmosphere*, edited by M.O. Andreae, and D.S. Schimel, J. Wiley and Sons, 1989.

Norman, J.M., R. Garcia, and S.B. Verma, Soil surface CO_2 fluxes and the carbon budget of a grassland, *J. Geophys. Res., 97*, 18,845–18,853, 1992.

NIST (National Institute of Science and Technology), *NIST Database 14 Mixture Property Database, version 9.08*, U.S. Department of Commerce, Oct. 1992.

Oldenburg, C.M., and K. Pruess, Simulation of propagating fronts in geothermal reservoirs with the implicit Leonard total variation diminishing scheme, *Geothermics, 29*, 1125, 2000.

Oldenburg, C.M., J.L. Lewicki, and R.P. Hepple, Near-surface monitoring strategies for carbon dioxide storage verification, Lawrence Berkeley National Laboratory Report *LBNL-54089*,

2003.

Oldenburg, C.M., and A.J.A. Unger, On leakage and seepage from geologic carbon sequestration sites: unsaturated zone attenuation, *Vadose Zone Journal*, 2, 287–296, 2003.

Oldenburg, C.M., and A.J.A. Unger, Coupled vadose zone and atmospheric surface-layer transport of CO_2 from geologic carbon sequestration seepage simulation, *Vadose Zone Journal*, 3, 848–857, 2004.

O'Leary, M.H., Carbon isotopes in photosynthesis, *Bioscience, 38*, 328–336, 1988.

Oskarsson, N., K. Palsson, H. Olafsson, and T. Ferreira, Experimental monitoring of carbon dioxide by low power IR-sensors: Soil degassing in the Funas Volcanic Centre, Azores, *J. Volcanol. Geotherm. Res., 92*, 195–207, 1999.

Osozawa, S. and S. Hasegawa, Diel and seasonal changes in carbon dioxide concentration and flux in an andisol, *Soil Science, 160*, 117–124, 1995.

Parada, C.B., A. Long, and S.N. Davis, Stable-isotopic compositions of soil carbon dioxide in the Tucson Basin, Arizona, U.S.A., *Isot. Geosci., 1*, 219–236, 1983.

Pruess, K., C. Oldenburg, and G. Moridis, TOUGH2 User's Guide Version 2.0, Lawrence Berkeley National Laboratory Report *LBNL-43134*, 197 pp., November 1999.

Radziemski, L. J., Richard W. Solarz, and Jeffrey A. Paisner, Laser Spectroscopy and Its Applications, *Optical Engineering Series No. 11*, Marcel Dekker, NY, 1987.

Reimer, G.M. Use of soil-gas helium concentrations for earthquake prediction: Limitations imposed by diurnal variation, *J. Geophys. Res., 85*, 3107–3114, 1980.

Rogie, J.D., D.M. Kerrick, M.L. Sorey, G. Chiodini, and D.L. Galloway, Dynamics of carbon dioxide emission at Mammoth Mountain, California, *Earth Planet. Sci. Lett., 188*, 535-541, 2001.

Rolston, D.E., Gas flux, in "Methods of Soil Analysis, 1, Physical and Mineralogical Methods," edited by A. Klute, *Am. Soc. Agron. Monogr., 9*, 1103–1119, 1986.

Salazar, J. M., P. A. Hernandez, N. M. Perez, G. Melian, J. Alvarez, F. Segura, and K. Notsu, Diffuse emission of carbon dioxide from Cerro Negro volcano, Nicaragua, Central America, *Geophys. Res. Lett., 22*, 4275–4278, 2001.

Schery, S. D., D. H. Gaeddert, and M. H. Wilkening, Factors affecting exhalation of radon from a gravelly sandy loam, *J. Geophys. Res., 89*, 7299–7309, 1984.

Schlessinger, M., *Infrared Technology Fundamentals*, *2nd Ed*., Revised and Expanded, Optical Engineering Series No.46, Marcel Dekker, Inc., New York, NY, 1995.

Shuler, P.J. and Y. Tang, Atmospheric CO_2 Monitoring Systems – A Critical Review of Available Techniques and Technology Gaps: Report for SMV Group, The CO_2 Capture Project (CCP), The Carbon Capture Project, 2002.

Singh, J.S. and S.R. Gupta, Plant decomposition and soil respiration in terrestrial ecosystems, *Bot. Rev., 43*, 449–528, 1977.

Slade, D.H., (editor), *Meteorology and Atomic Energy 1968*, Chapter 2, U.S. Atomic Energy Commission, 1968.

Sorey, M.L., W.C. Evans, B.M. Kennedy, C.D. Farrar, L.J. Hainsworth, and B. Hausback, Carbon dioxide and helium emissions from a reservoir of magmatic gas beneath Mammoth Mountain, California, *J. Geophys. Res., 103*, 15,303-15,323, 1998.

Sorey, M.L., C.D. Farrar, W.C. Evans, D.P. Hill, R.A. Bailey, J.W. Hendley II, and P.H. Stauffer, Invisible CO_2 gas killing trees at Mammoth Mountain, California, U.S. Geological Survey Fact Sheet 172–96, 4pp., 1996. http://wrgis.wr.usgs.gov/fact-sheet/fs172-96/.

Southon, J.R., J.S. Vogel, S.E. Trumbore, J.C. Davis, M.L. Roberts, M.W. Caffee, R.C. Finkel, I.D. Proctor, D.W. Heikkinen, A.J. Berno, and R.S. Hornady, Progress in AMS measurements at the LLNL spectrometer, *Radiocarbon, 34*, 473–477, 1993.

Spycher, N., K. Pruess, and J. Ennis-King, CO_2-H_2O mixtures in geological sequestration of CO_2. Assesment and calculation of mutual solubilities from 12 to 100 ˚C and up to 600 bar, *Geochimica et Cosmochimica Acta*, *67*(16), 3015–3031, 2003.

Trumbore, S., Age of soil organic matter and soil respiration: radiocarbon constraints on belowground dynamics, *Ecological Applications, 10*, 399–411, 2000.

USGS, Measuring volcanic gases: emission rates of sulfur dioxide and carbon dioxide in volcanic plumes, 2000a. http://volcanoes.usgs.gov/About/What/Monitor/Gas/plumes.html.

USGS, Measuring volcanic gases: soil efflux, 2000b. http://volcanoes.usgs.gov/About/What/Monitor/Gas/soil.html.

van Genuchten, M.T., A closed-form equation for predicting the hydraulic conductivity of unsaturated soils, *Soil Sci. Soc. Am. J.*, *44*, 892–898, 1980.

Vargaftik, N.B., Y.K. Vinogradov, and V.S. Yargin, *Handbook of Physical Properties of Liquids and Gases, Third Edition*, Begell House, New York, 1359 pp., 1006, 1996.

Werner, C., S.L. Brantley, and K. Boomer, CO_2 emissions related to the Yellowstone volcanic system 2. Statistical sampling, total degassing, and transport mechanisms, *J. Geophys. Res., 105*, 10,831-10,846, 2000.

Wiant, H.V., Influence of temperature on the rate of soil respiration, *J. For., 65*, 489–490, 1967a.

Wiant, H.V., Influence of moisture content on the "soil respiration", *J. For., 65*, 902–903, 1967b.

Wood, W.W. and M.J. Petraitis, Origin and distribution of carbon dioxide in the unsaturated zone of the southern high plains of Texas, *Water Resour. Res., 20*, 1193–1208, 1984.

Wood, B.D., C.K. Keller, and D.L. Johnstone, In situ measurement of microbial activity and contrals on microbial CO_2 production in the unsaturated zone, *Water Resour. Res., 29*, 647–659, 1993.

TABLES

Table 4.1. Properties of the coupled subsurface–surface-layer model system.

Property	Value
Subsurface	
Subsurface region extent (x x y x z)	1 km x 1 m x 124 m
Discretization (Nx x Ny x Nz)	67 x 1 x 31
Standard deviation of log k	0.70
Minimum, maximum k	1×10^{-14},1×10^{-10} m^2
Correlation length of k in Y-, Z-direction	45, 1 m
Porosity (ϕ)	0.2
Infiltration rate (i)	0.0 cm yr^{-1}
Temperature (isothermal)	15^{o}C
CO_2 source location (x, y)	293.5 m, -86 m
Source CO_2 migration rate	$1. \times 10^{-4}$, $1. \times 10^{-5}$, $1. \times 10^{-6}$ kg s^{-1}
Residual water sat. (S_{lr})	0.1
Residual gas sat. (S_{gr})	0.01
van Genuchten (1980) α	1×10^{-4} Pa^{-1}
van Genuchten (1980) m	0.2
Surface Layer	
Surface-layer region extent (x x y x z)	1 km x 1 m x 62 m
Discretization (Nx x Ny x Nz)	67 x 1 x 31
Pressure in surface layer	1 bar
Temperature	15 ^{o}C
Velocity profile	Logarithmic
Reference velocity at z = 10 m	1 or 3 m s^{-1}
Friction velocity for v = 1 m s^{-1}	0.0861 m s^{-1}
Friction velocity for v = 3 m s^{-1}	0.261 m s^{-1}
Roughness length (z_0)	0.1 m

Table 7.1. Chemical and isotopic signatures related to CO_2 derived from different sources.

CO_2 source	$\delta^{13}C_{CO2}$ ‰	$\Delta^{14}C_{CO2}$ ‰	Near-surface CO_2 conc.	CO_2 conc. profile with depth	O_2 conc. profile with depth
Atmosphere	-7	70	Low	–	–
Plant root respiration and oxidative decay of young soil organic matter	C_3: -24 to -38 C_4: -6 to -19	≥70	Low to moderate	Increasing through soil zone	Decreasing through soil zone
Oxidative decay of ancient organic matter	C_3: -24 to -38 Aquatic/C_4: -6 to -19 Also age dependent	Highly depleted to absent, depending on age	Low	Increasing potentially through vadose zone	Decreasing potentially through vadose zone
Marine carbonate rocks	0 ± 4	absent	Low	Increasing through vadose zone	No effect
Geothermal	-2 to -6	absent	Moderate to high	Increasing through vadose zone	No effect

Conc., C_3, and C_4, refer to concentration, C_3 plants, and C_4 plants. All near-surface concentrations given are general estimates; these concentrations will be strongly dependent on the magnitude of the CO_2 flux.

Table 7.2. *Properties of different case scenarios used in Monte Carlo simulations.*

Case	Permeability	*x/A*	*P(H)*
1	Homogeneous/isotropic	0.1	0.1
2	Homogeneous/isotropic	0.01	0.1
3	Homogeneous/isotropic	0.001	0.1
4	Homogeneous/isotropic	0.1	0.9
5	Homogeneous/isotropic	0.01	0.9
6	Homogeneous/isotropic	0.001	0.9
7	Heterogeneous/isotropic	0.1	0.1
8	Heterogeneous/isotropic	0.01	0.1
9	Heterogeneous/isotropic	0.001	0.1
10	Heterogeneous/isotropic	0.1	0.9
11	Heterogeneous/isotropic	0.01	0.9
12	Heterogeneous/isotropic	0.001	0.9

Table 7.3. *Mean (μ) and standard deviation (σ) of number of measurements (n) required to detect a soil CO_2 flux anomaly within a sampling area and the associated CO_2 flux threshold for different case scenarios.*

Case	μ g $m^{-2}d^{-1}$	σ g $m^{-2}d^{-1}$	Threshold g $m^{-2}d^{-1}$
1	5415	3029	28
2	>20,000	na	na
3	>20,000	na	na
4	1869	1784	29
5	19,984	256	28
6	>20,000	na	na
7	3407	1919	38
8	>20,000	na	na
9	>20,000	na	na
10	1267	1253	38
11	19,984	256	45
12	>20,000	na	na

FIGURES

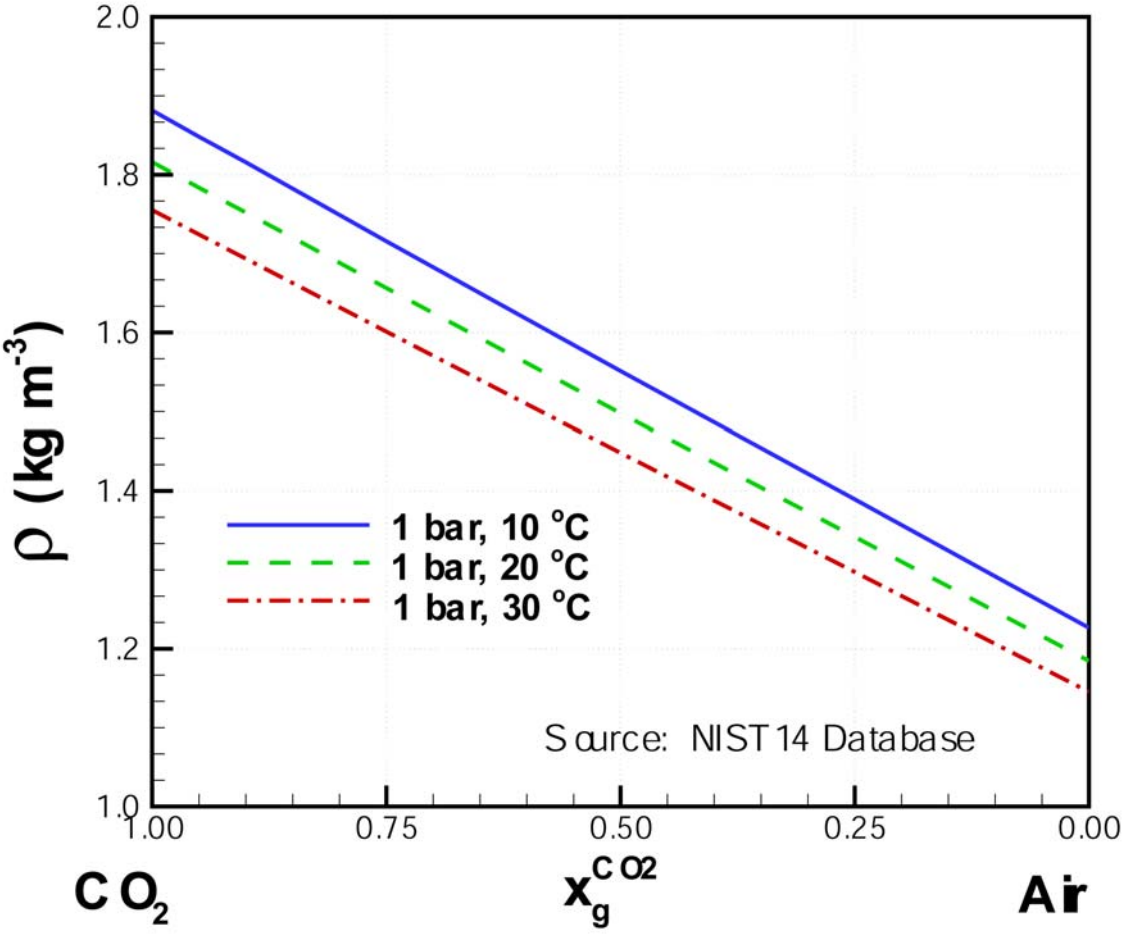

Figure 3.1. Density as a function of concentration (mole fraction) in the system CO_2-air.

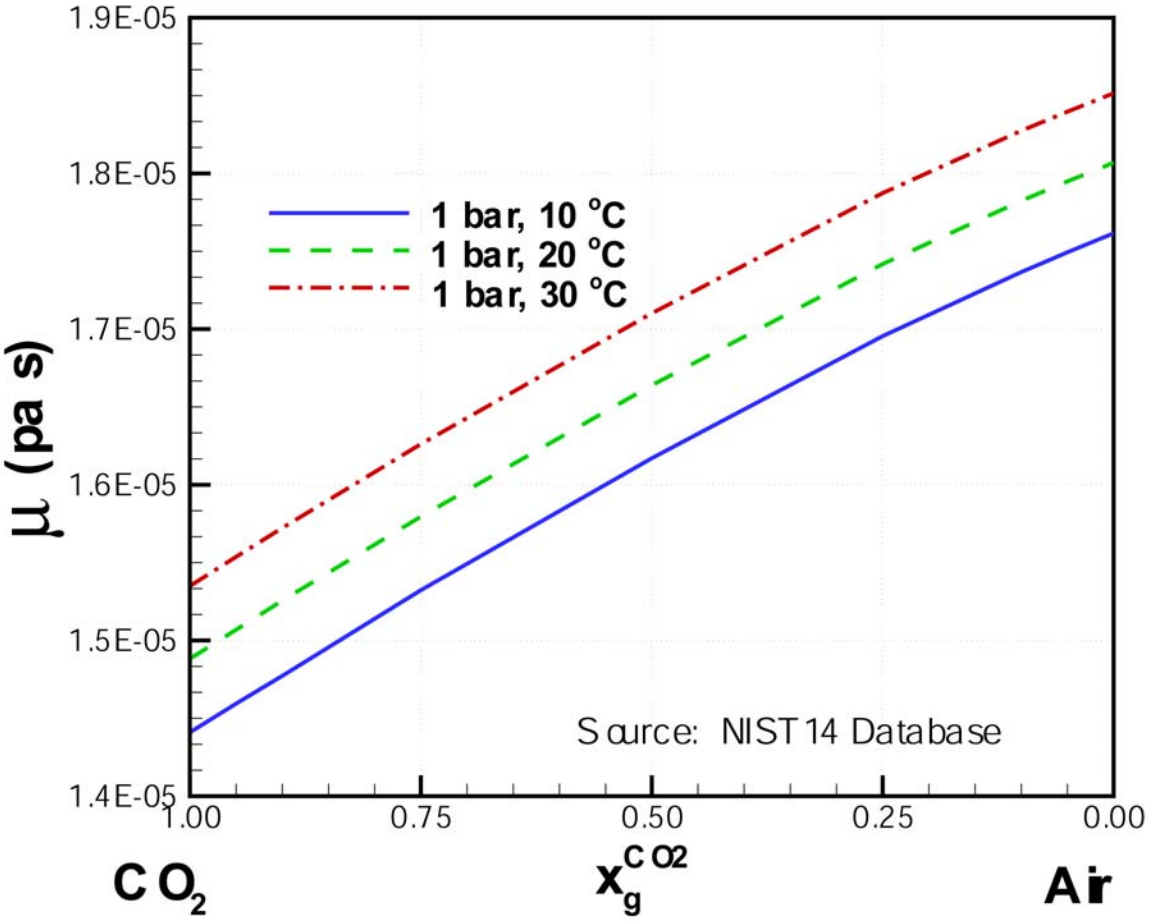

Figure 3.2. Viscosity as a function of concentration (mole fraction) in the system CO_2-air.

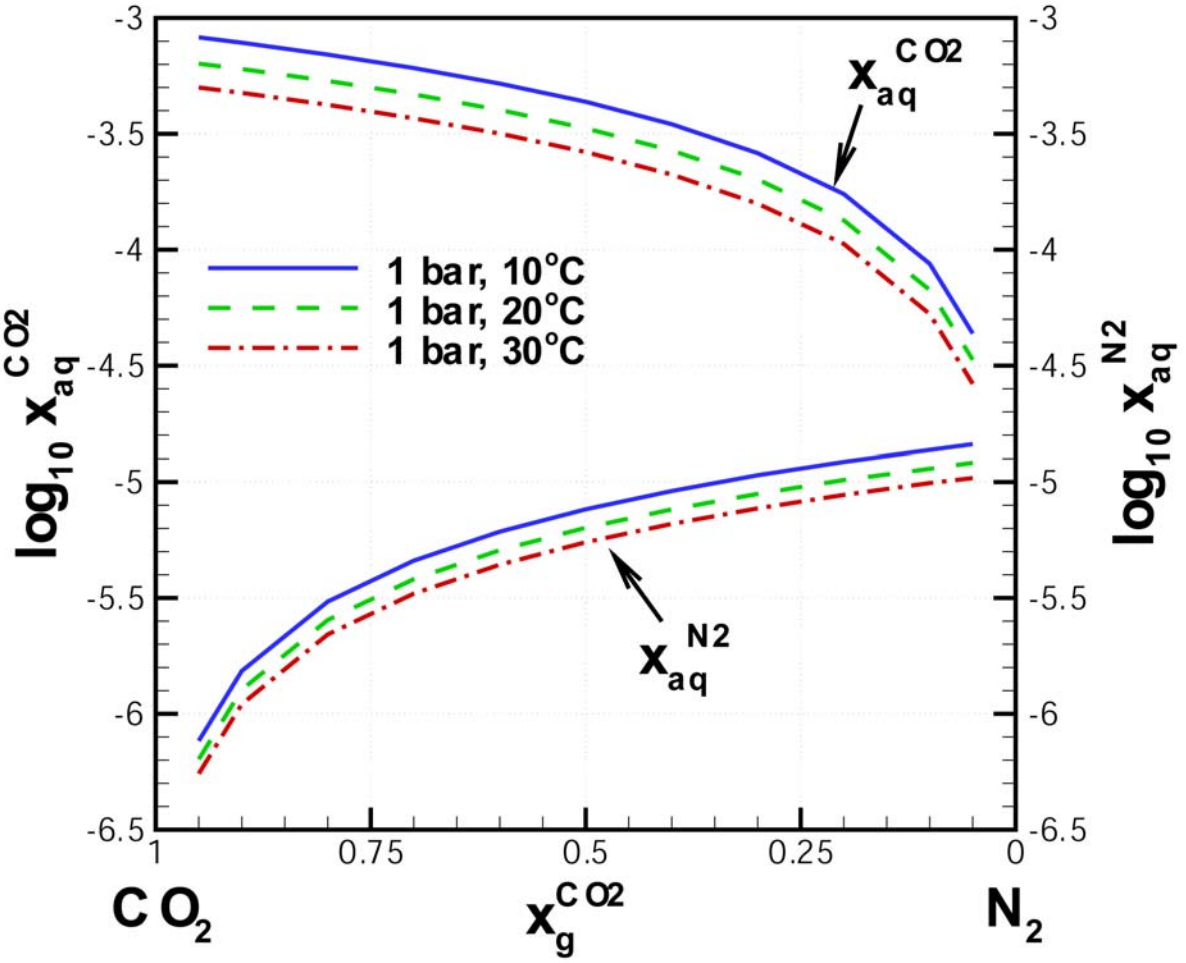

Figure 3.3. Solubility of CO_2 and N_2 in water (mole fraction) in gas and aqueous phases.

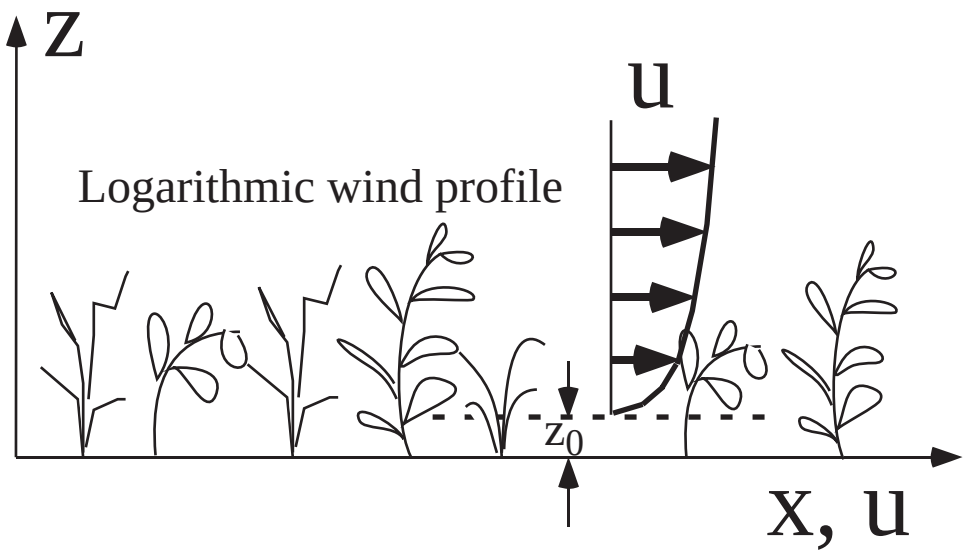

Figure 4.1 Logarithmic velocity profile for atmospheric surface layer.

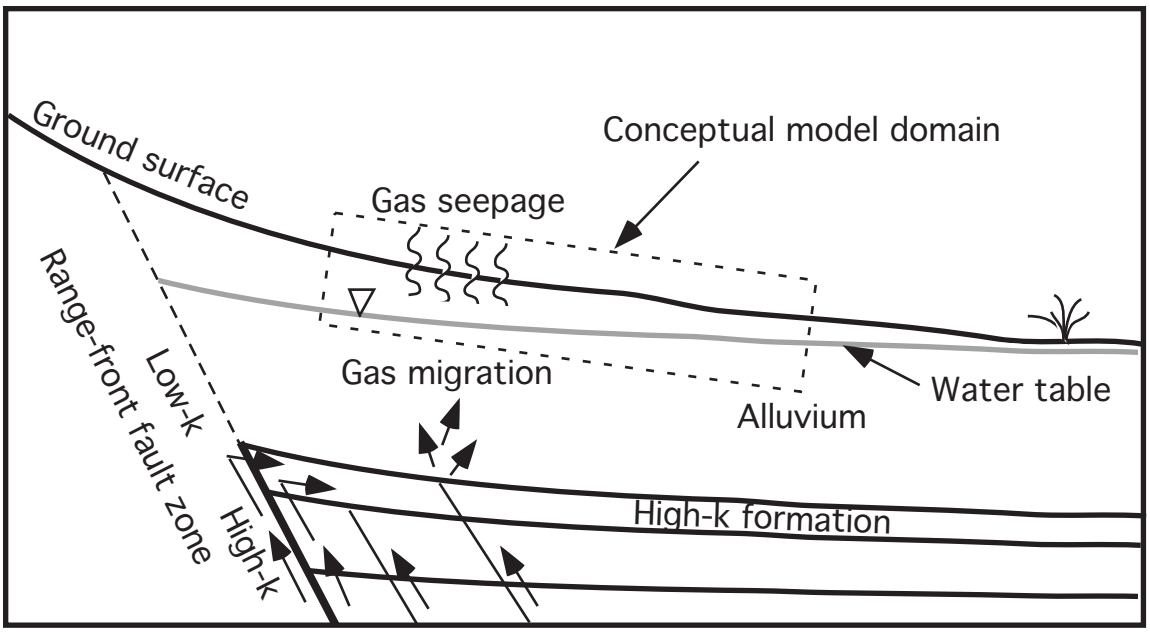

Figure 4.2. Conceptual model for gas migration from a deep hidden geothermal system.

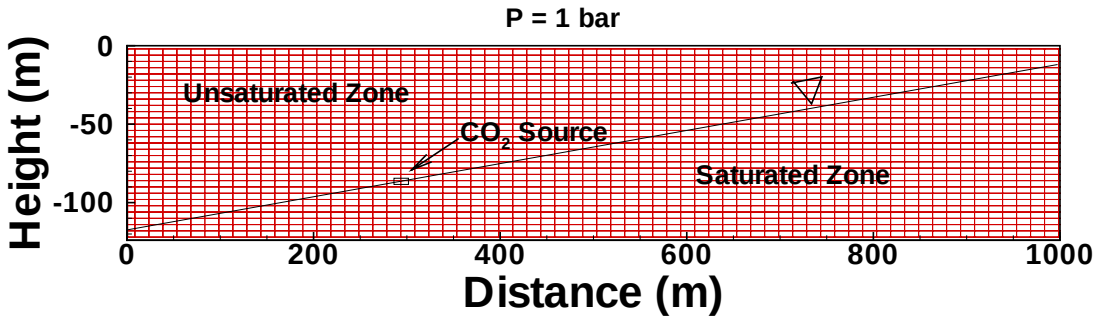

Figure 4.3. Grid and boundary conditions for the subsurface model system. Note vertical exaggeration, tilt is actually only six degrees relative to horizontal.

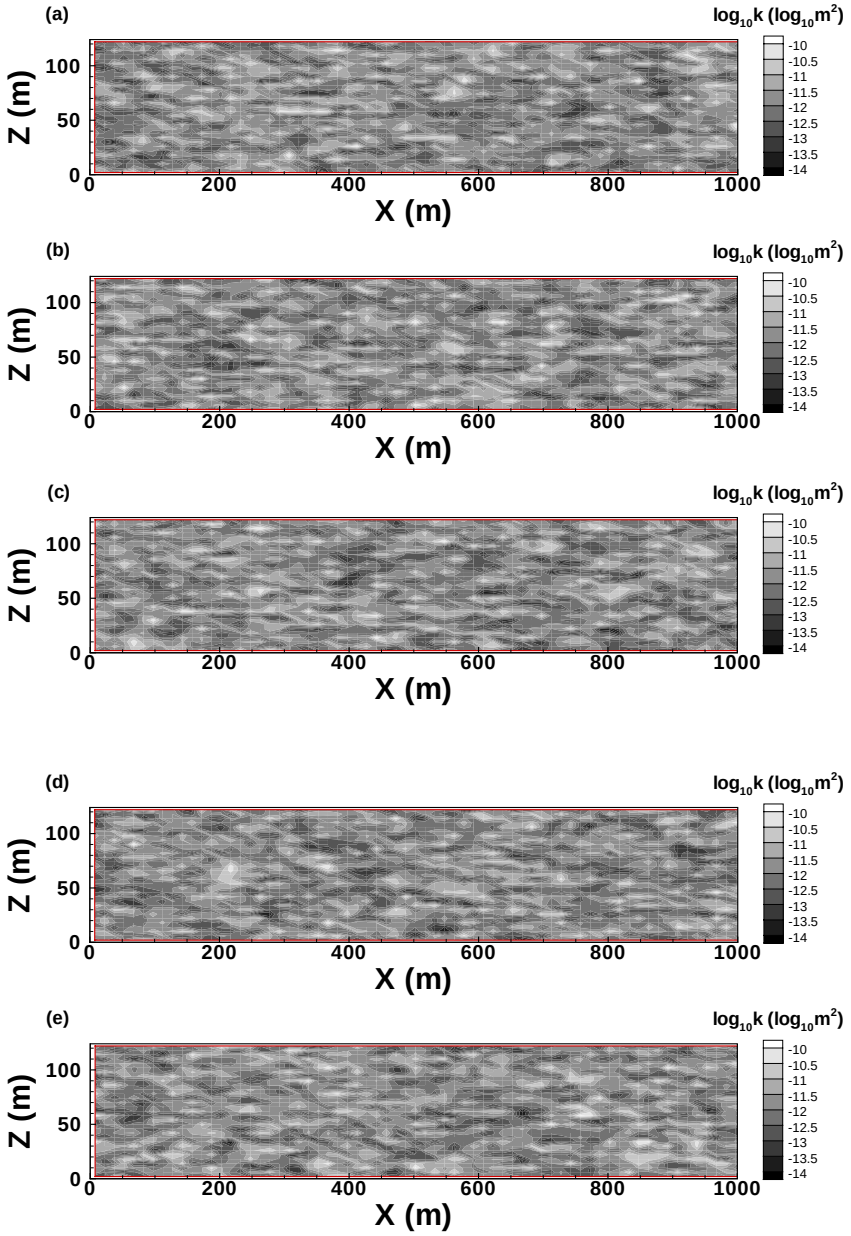

Figure 4.4. Five realizations (A–E) of permeability heterogeneity for the alluvial fan system.

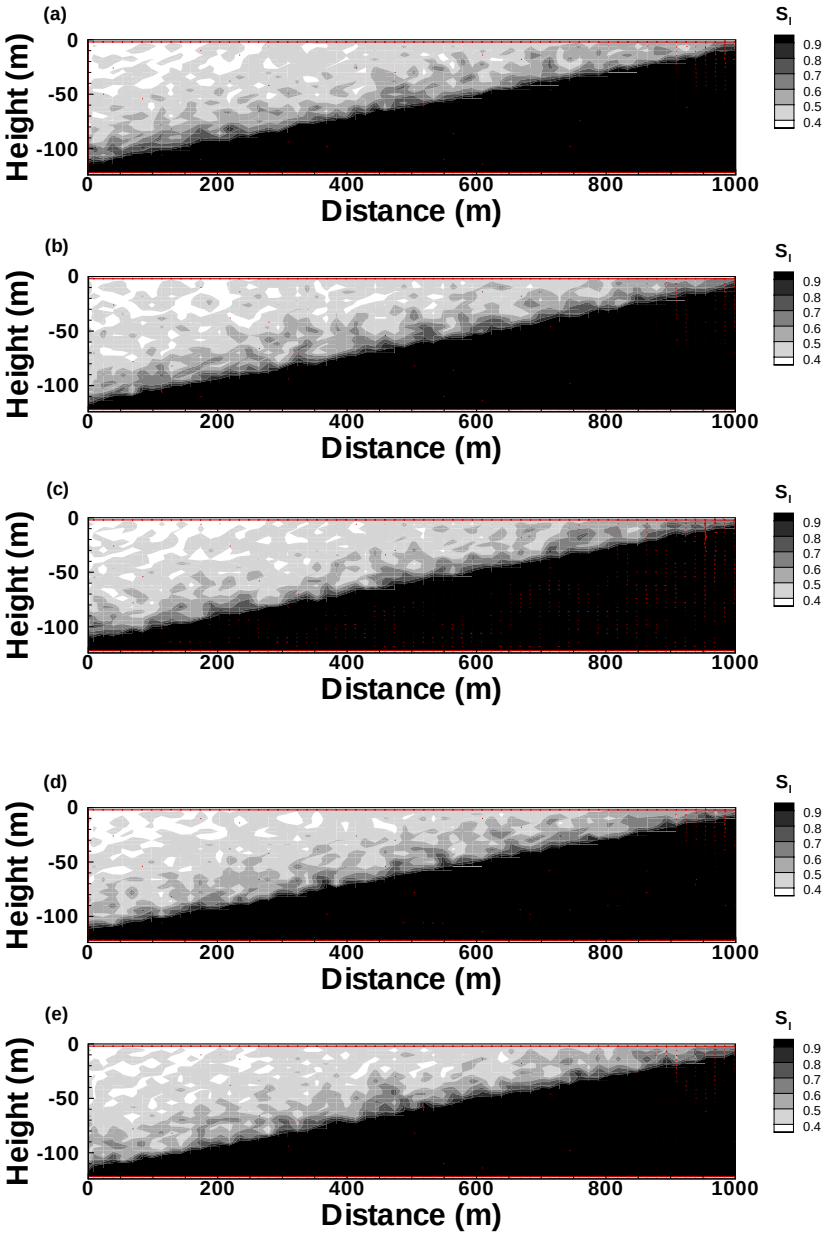

Figure 4.5. Initial liquid saturation for the five realizations (A–E).

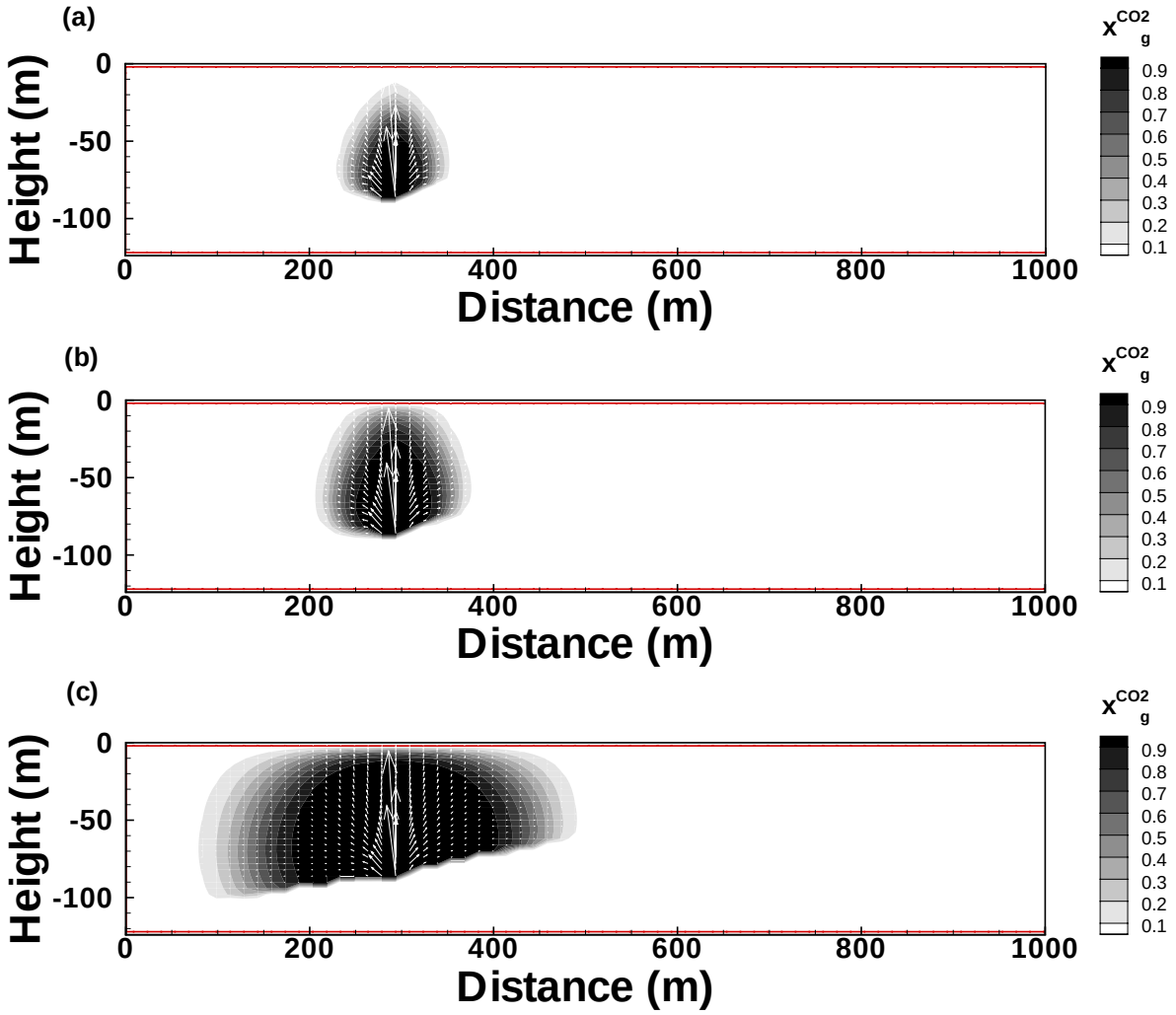

Figure 4.6. Subsurface CO_2 concentrations (mole fraction) at t = (a) 0.5, (b) one, and (c) ten years for the homogeneous permeability field and high CO_2 source flux (576 g $m^{-2}d^{-1}$).

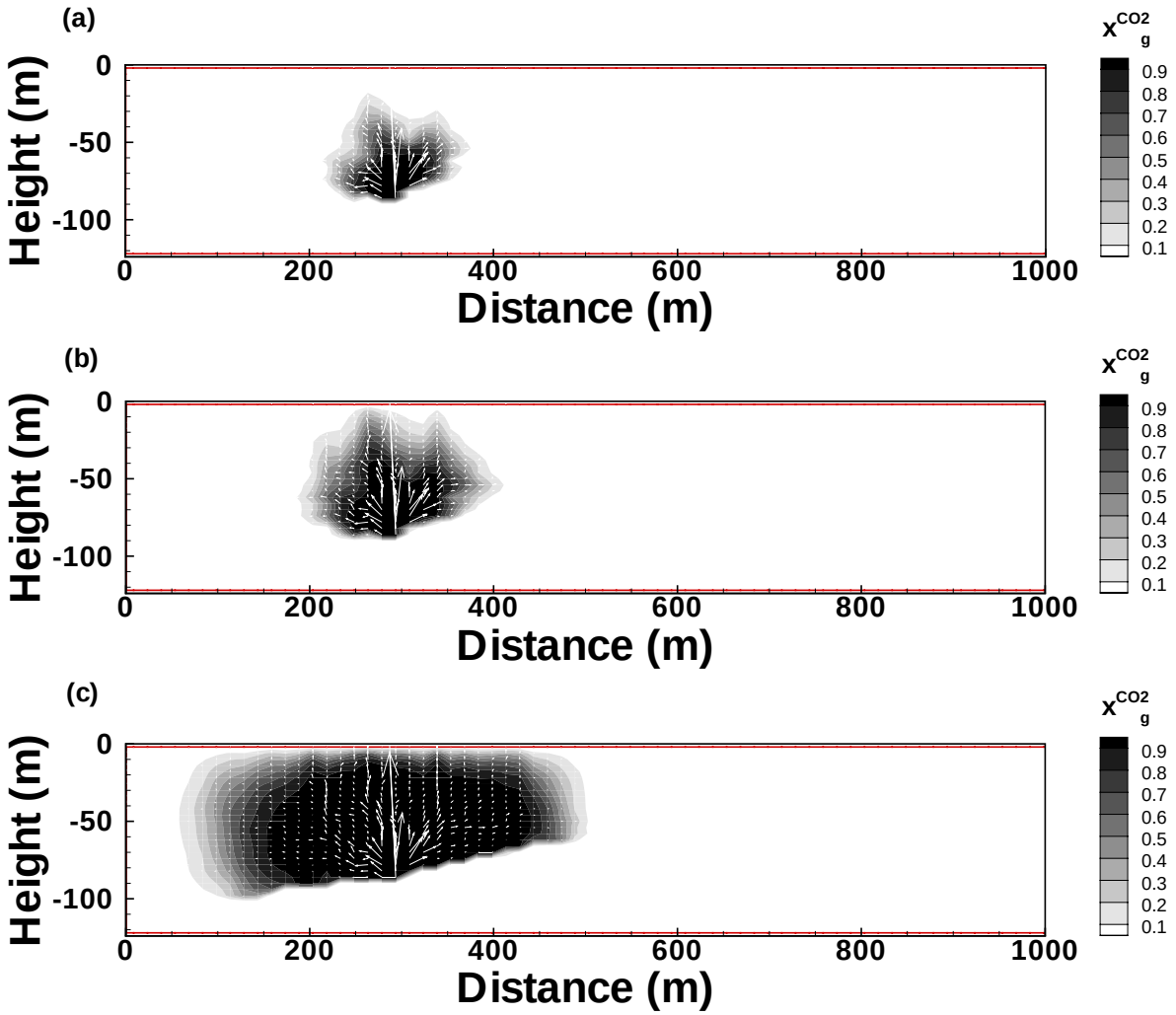

Figure 4.7. Subsurface CO_2 concentrations (mole fraction) at t = (a) 0.5, (b) one, and (c) ten years for permeability realization A and high CO_2 source flux (576 g $m^{-2}d^{-1}$).

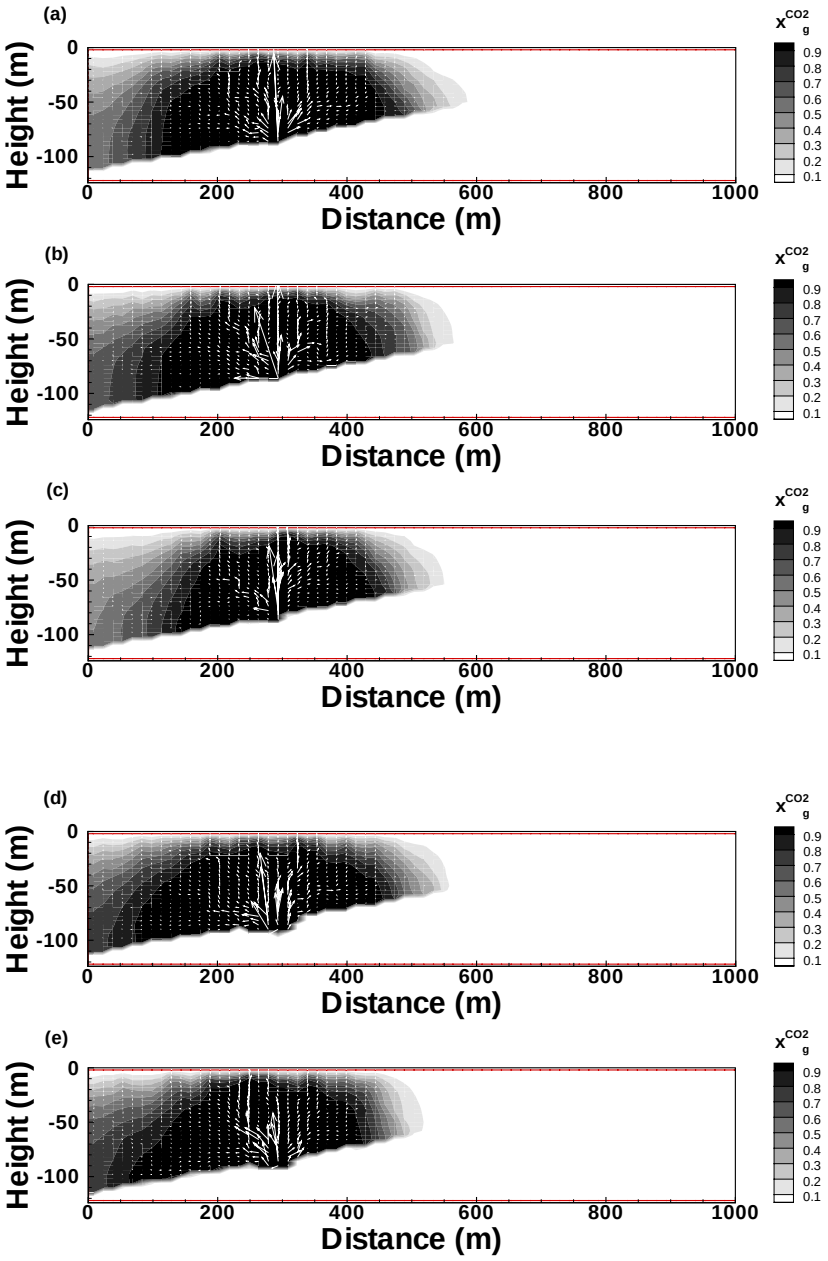

Figure 4.8. Subsurface CO_2 concentrations (mole fraction) at t = 200 years for five permeability realizations (A–E) and high CO_2 source flux (576 g m^{-2} d^{-1}).

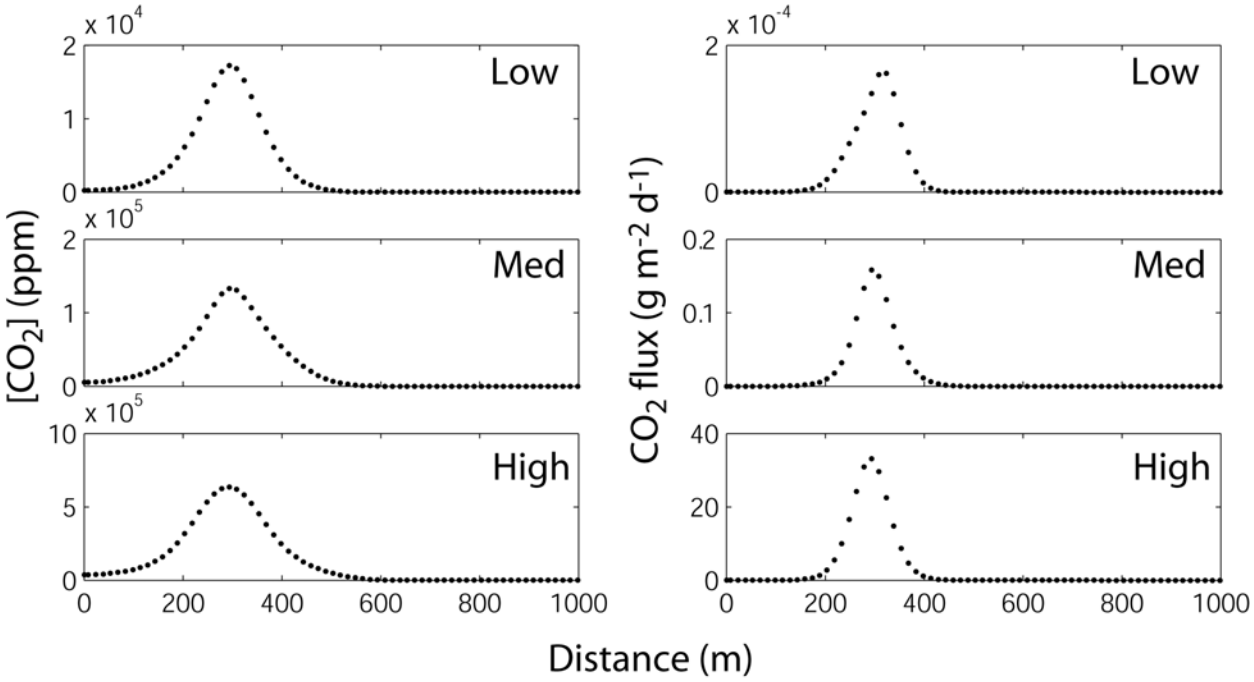

Figure 4.9. Horizontal profiles of shallow subsurface CO_2 concentration ([CO_2], 3 m depth) and surface CO_2 flux for low (5.76 g m^{-2} d^{-1}), medium (57.6 g m^{-2} d^{-1}), and high (576 g m^{-2} d^{-1}) CO_2 source fluxes, homogeneous isotropic permeability, and t = 200 years.

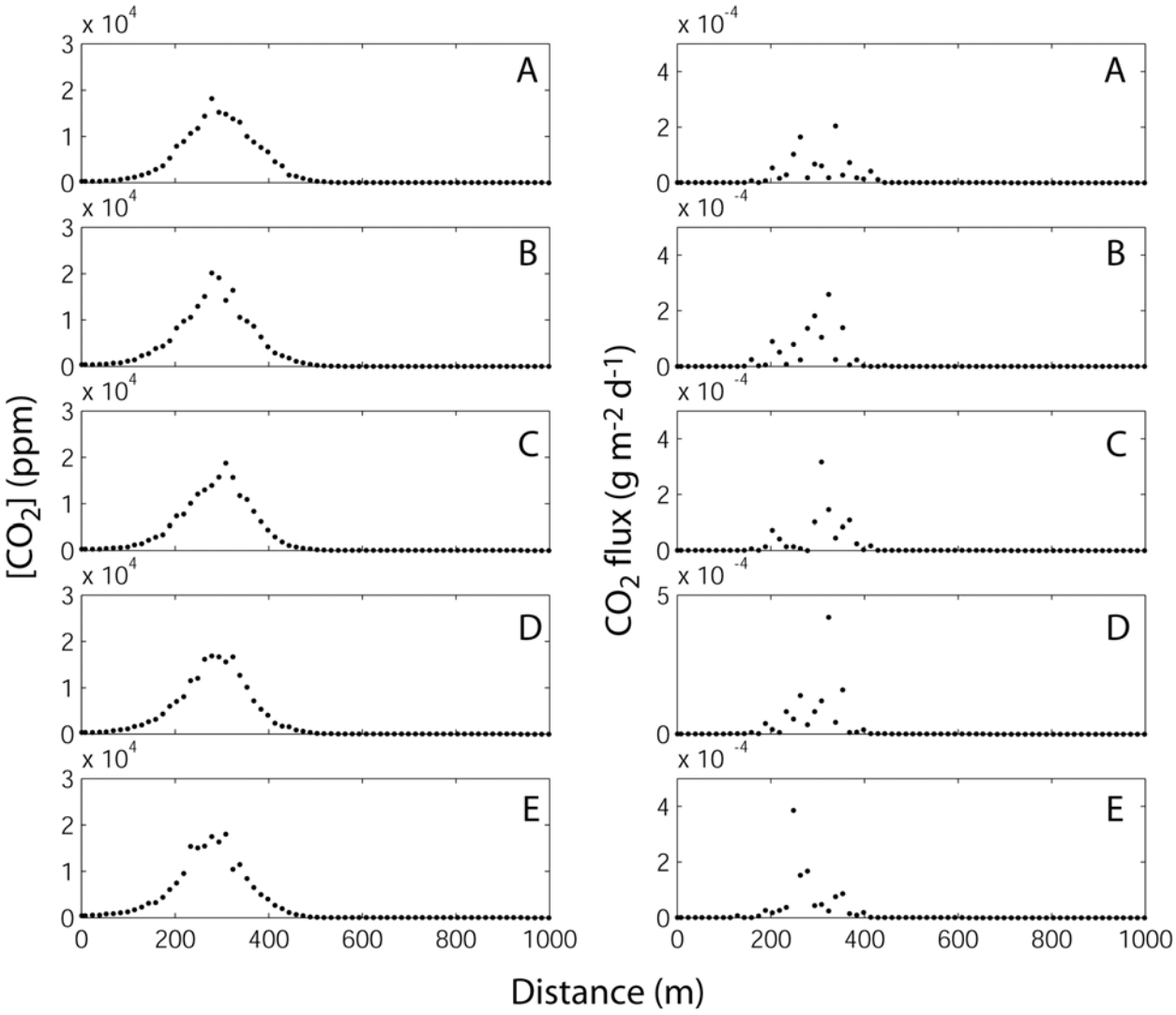

Figure 4.10. Horizontal profiles of shallow subsurface CO_2 concentration ([CO_2], 3 m depth) and surface CO_2 flux for low (5.76 g $m^{-2}d^{-1}$) CO_2 source flux, heterogeneous isotropic permeability realizations A-E, and t = 200 years.

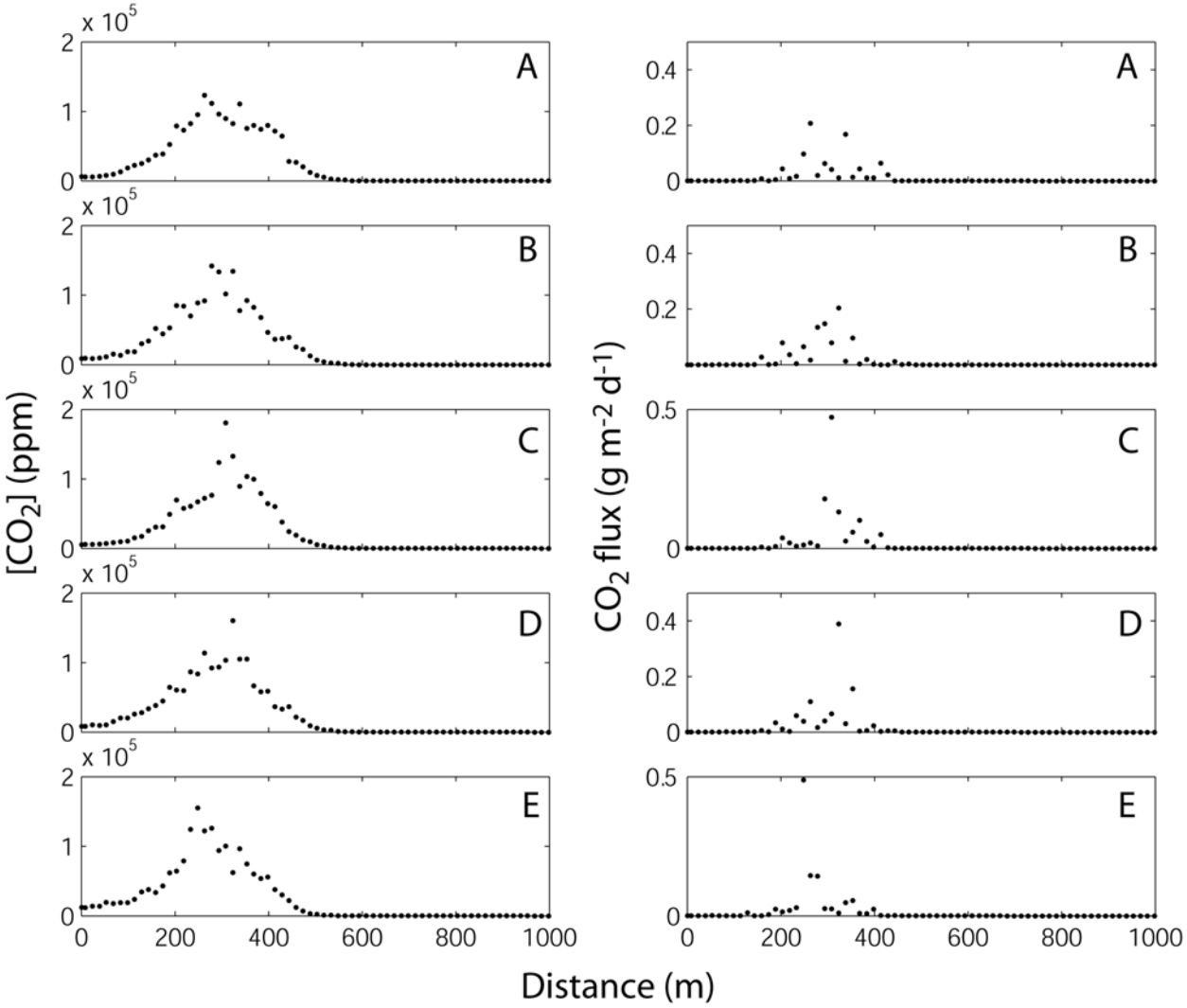

Figure 4.11. Horizontal profiles of shallow subsurface CO_2 concentration ([CO_2], 3 m depth) and surface CO_2 flux for medium (57.6 g $m^{-2}d^{-1}$) CO_2 source flux, heterogeneous isotropic permeability realizations A-E, and t = 200 years.

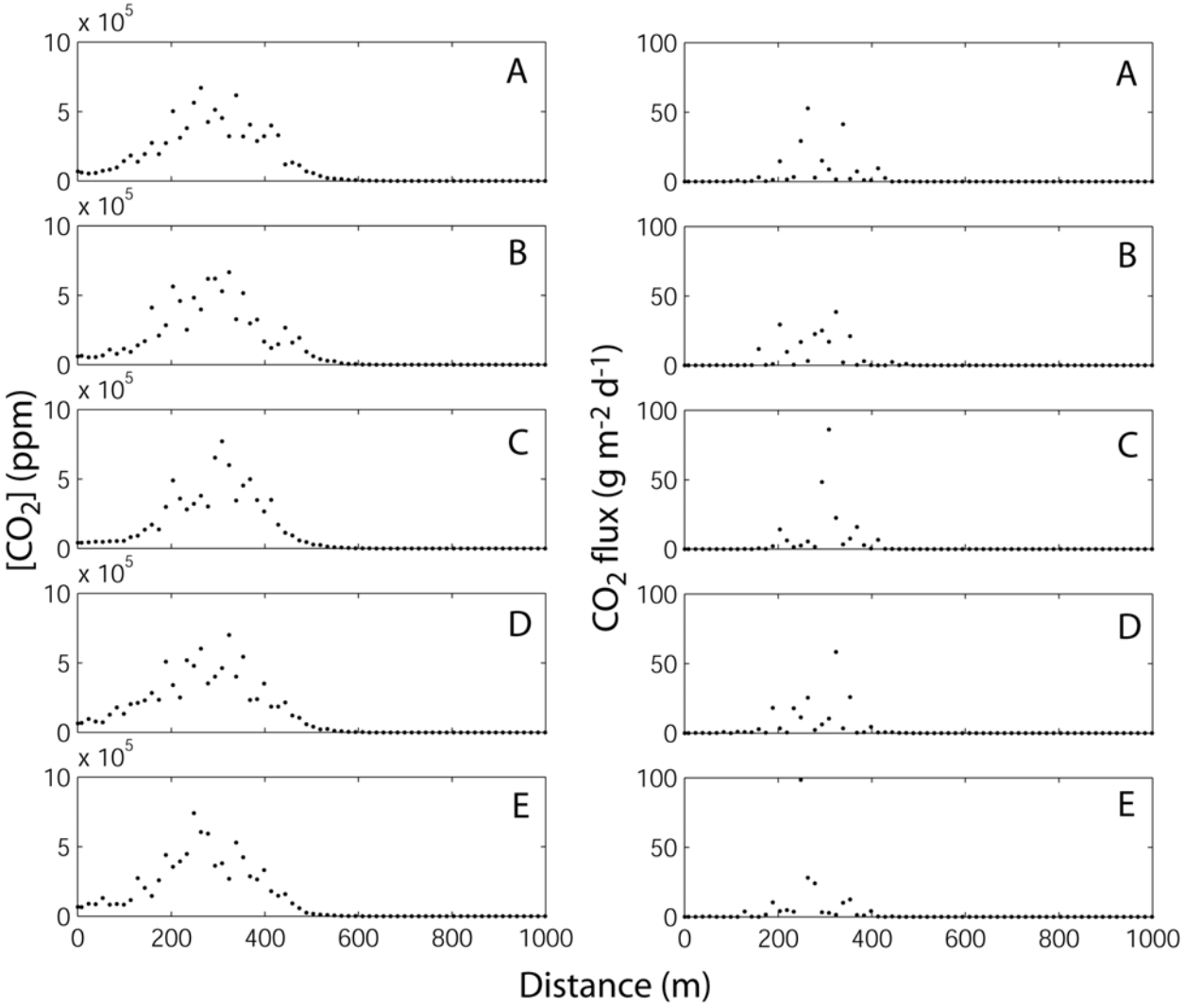

Figure 4.12. Horizontal profiles of shallow subsurface CO_2 concentration ([CO_2], 3 m depth) and surface CO_2 flux for high (576 g $m^{-2}d^{-1}$) CO_2 source flux, heterogeneous isotropic permeability realizations A-E, and t = 200 years.

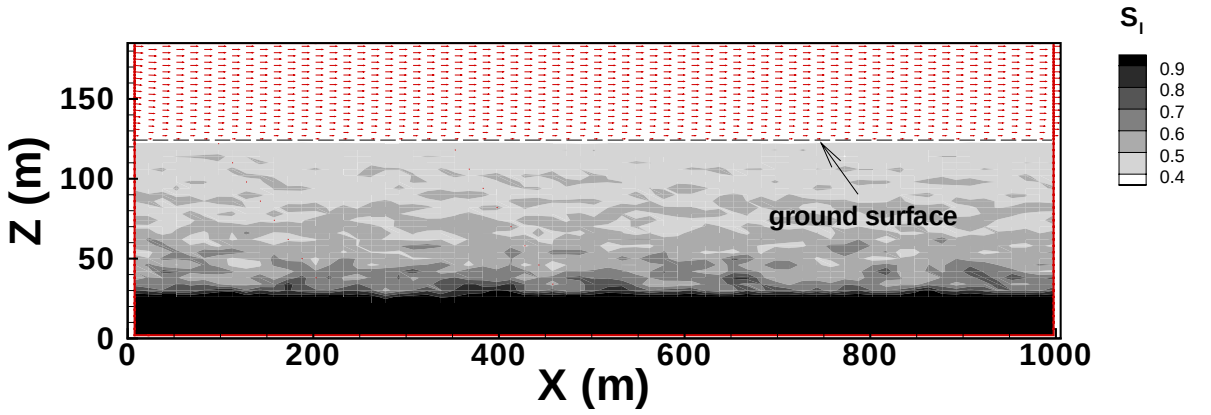

Figure 4.13. Initial liquid saturation and wind velocity for the coupled subsurface-surface layer system with heterogeneous permeability for subsurface.

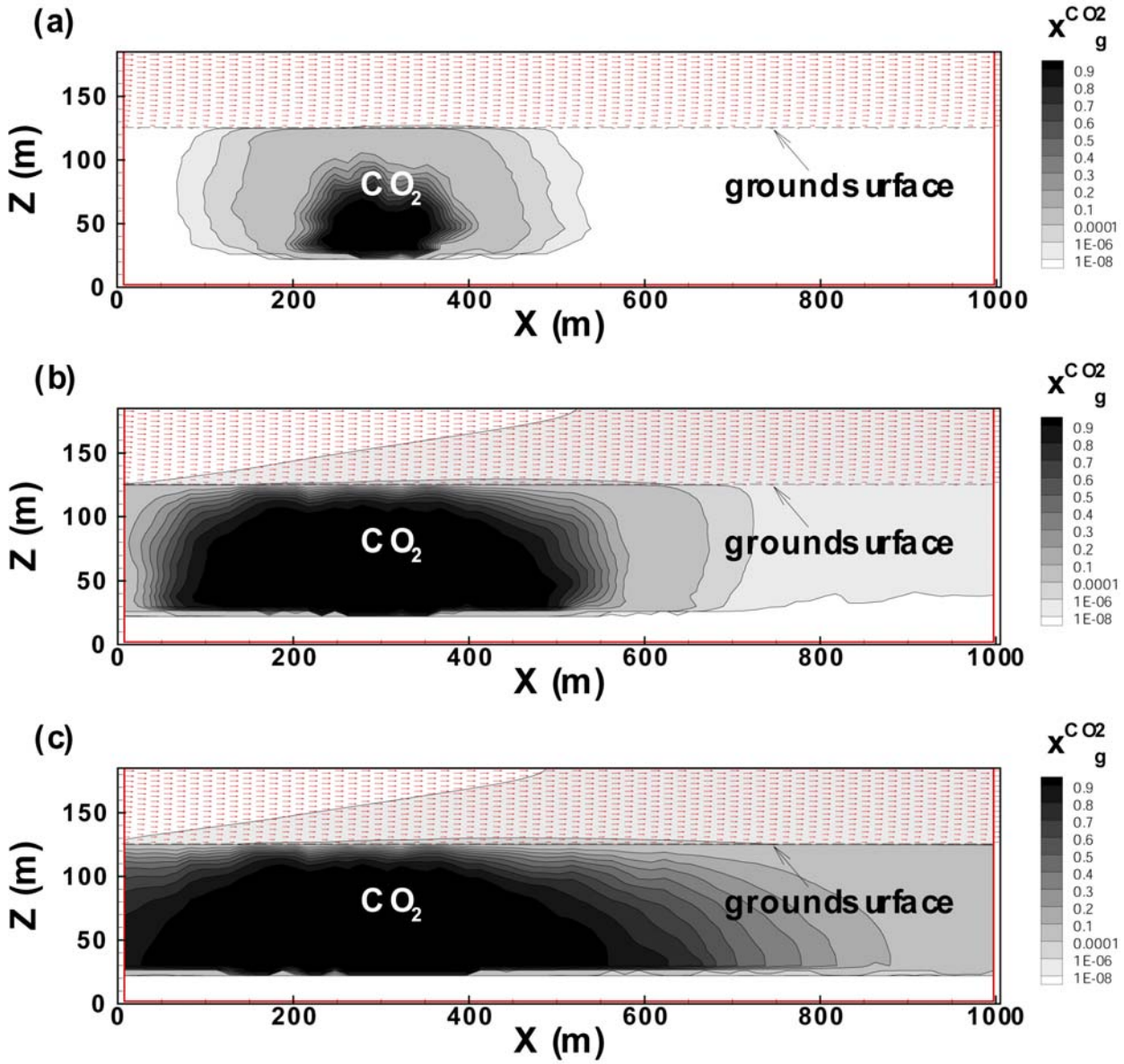

Figure 4.14. Coupled CO_2 subsurface migration and surface-layer mixing at 1, 10, and 200 years after CO_2 migration begins for wind velocity of 3 m s^{-1} and permeability realization A in a horizontal system.

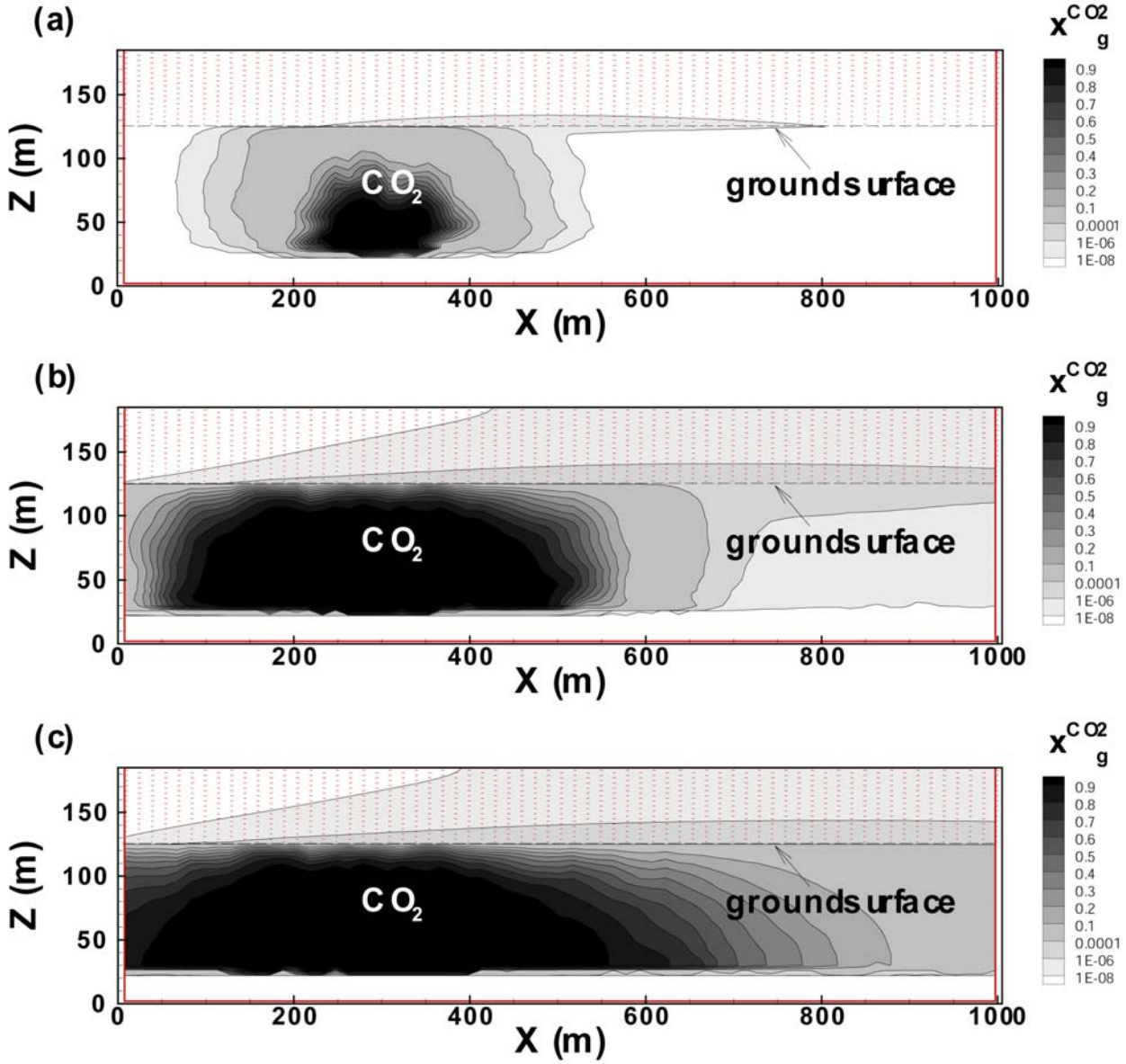

Figure 4.15. Coupled CO_2 subsurface migration and surface-layer mixing at 1, 10, and 200 years after CO_2 migration begins for wind velocity of 1 m s^{-1} and permeability realization A in a horizontal system.

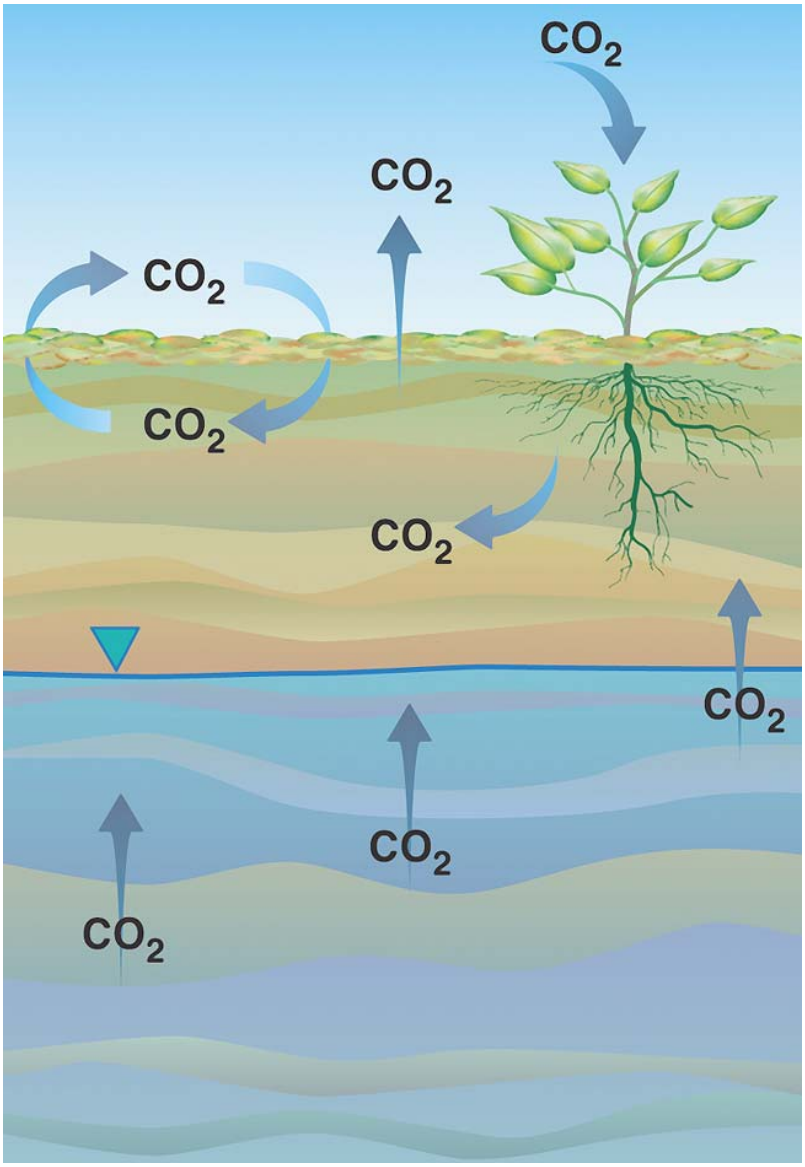

Figure 5.1. Soil CO_2 sources and sinks, showing from left-right, top-bottom, exchange with the atmosphere, production by decay of soil organic matter, photosynthetic uptake by plants, and production by root respiration, groundwater degassing, oxidation of sub-soil organic matter, and deep degassing.

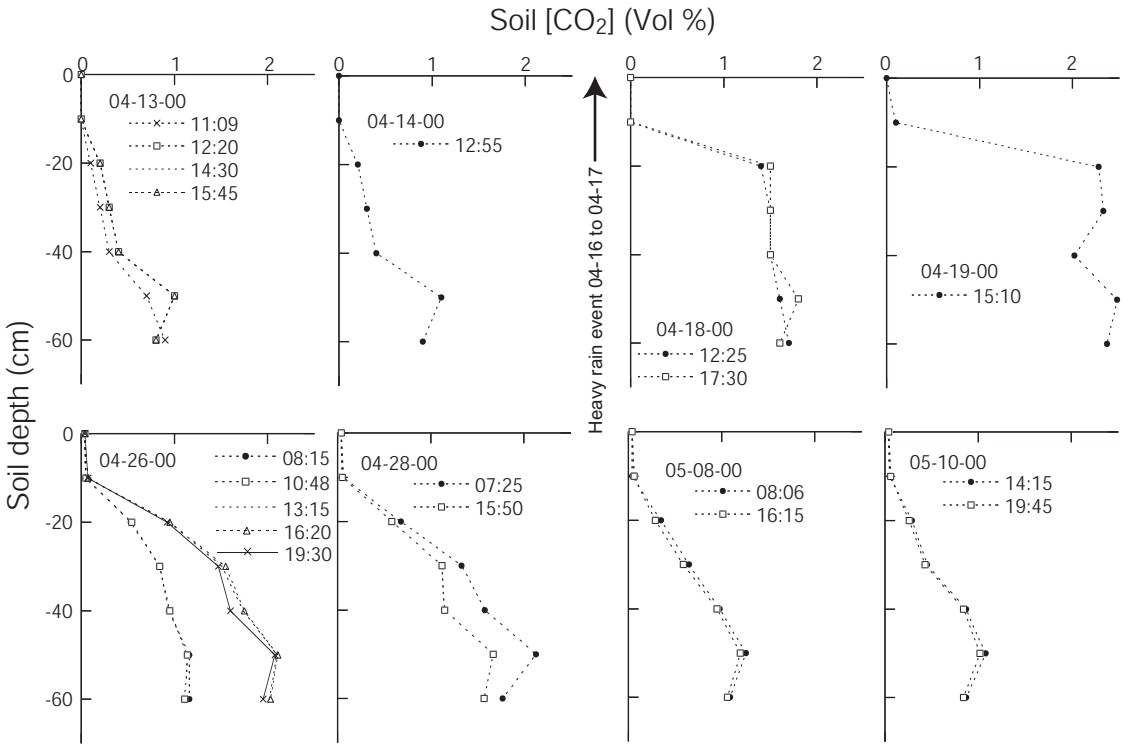

Figure 5.2. Repeated measurements of a soil CO_2 concentration profile in central California over a month-long period (modified from Lewicki et al., 2003). Measurement dates and times and the timing of a heavy rain event are shown. Temporal variability of soil CO_2 concentration is due to change in soil CO_2 production rates due to changes in soil temperature and water content. For example, increase in soil CO_2 concentrations is observed each day from morning to afternoon measurement times due to increasing soil respiration rates with soil temperature. Also, soil CO_2 concentrations increased following a heavy rain event (04-16-00 to 04-17-00) due to increasing soil respiration rates and/or decreasing loss of CO_2 to the atmosphere with increasing soil water content.

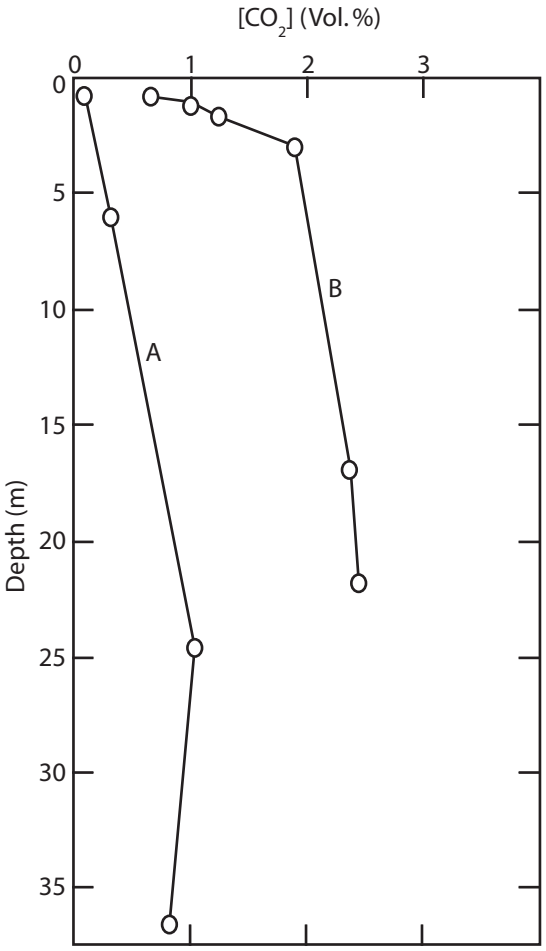

Figure 5.3. Profiles (A and B) of CO_2 concentration with depth in the unsaturated zone above the Ogallala aquifer system of Texas (modified from Wood and Petraitis, 1984). Increase in CO_2 concentration with depth was interpreted to result from production of CO_2 by oxidative decay of particulate organic carbon. The water table at sites A and B was ~51 and 77 m below the surface.

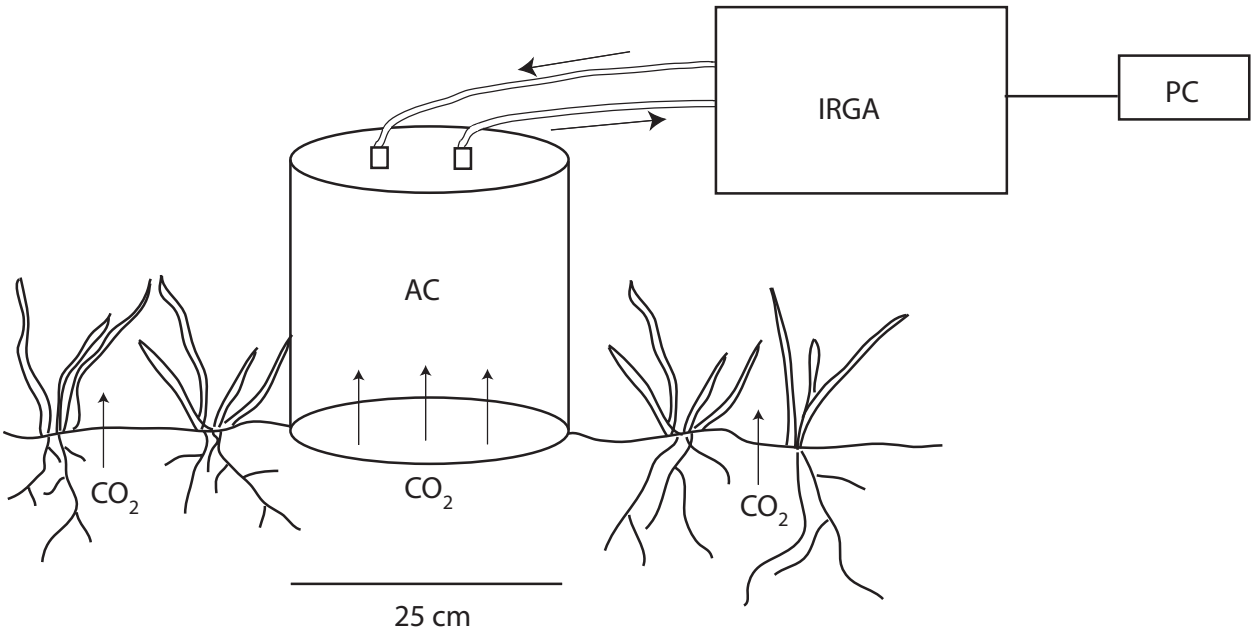

Figure 6.1. Schematic diagram of an accumulation chamber (AC) measurement system of soil CO_2 flux. The air contained in the AC is circulated through the AC and the IRGA and the rate of change of CO_2 concentration in the AC is measured by the IRGA and recorded by the PC.

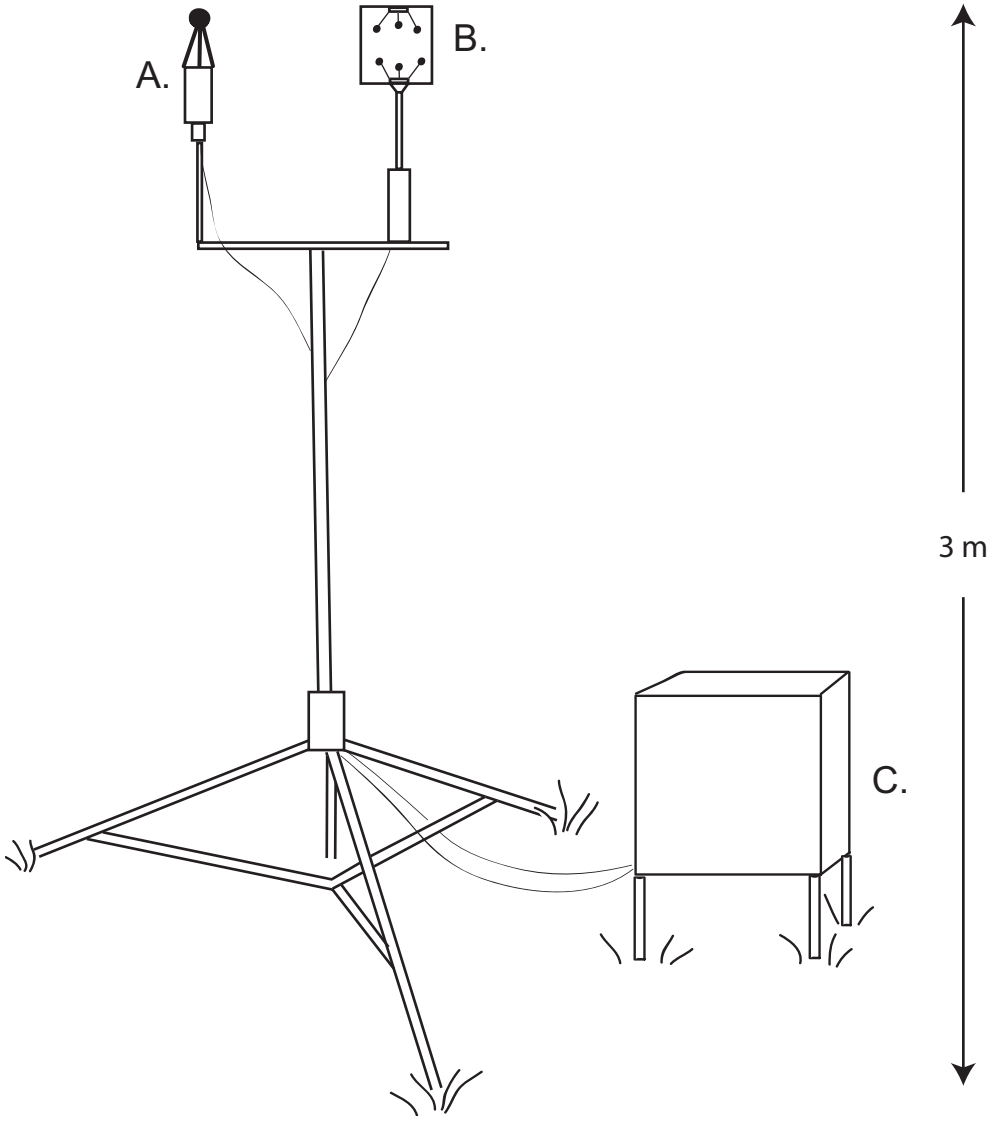

Figure 6.2. Schematic diagram of an eddy correlation (EC) instrumentation tower to measure surface CO2 flux. An (A) open path IRGA, (B) high frequency response sonic anemometer, and (C) box containing power source and datalogger/PC are shown.

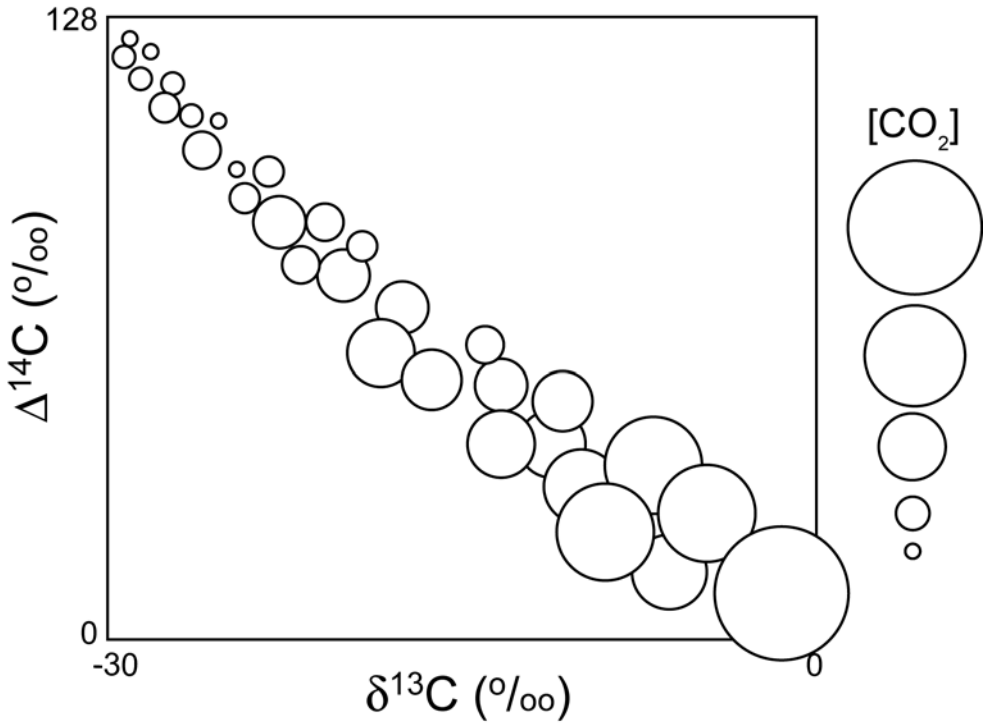

Figure 7.1. Bubble plot of $\Delta^{14}C$ versus $\delta^{13}C$ compositions of soil CO_2 showing idealized mixing trend between soil gas with relatively low CO_2 concentration ([CO_2]) and $\delta^{13}C$ and high $\Delta^{14}C$(young biogenic carbon dominated) and soil gas with relatively high CO_2 concentration, $\delta^{13}C$ and low $\Delta^{14}C$ (geothermal carbon dominated). Bubble size scales with soil gas CO_2 concentration.

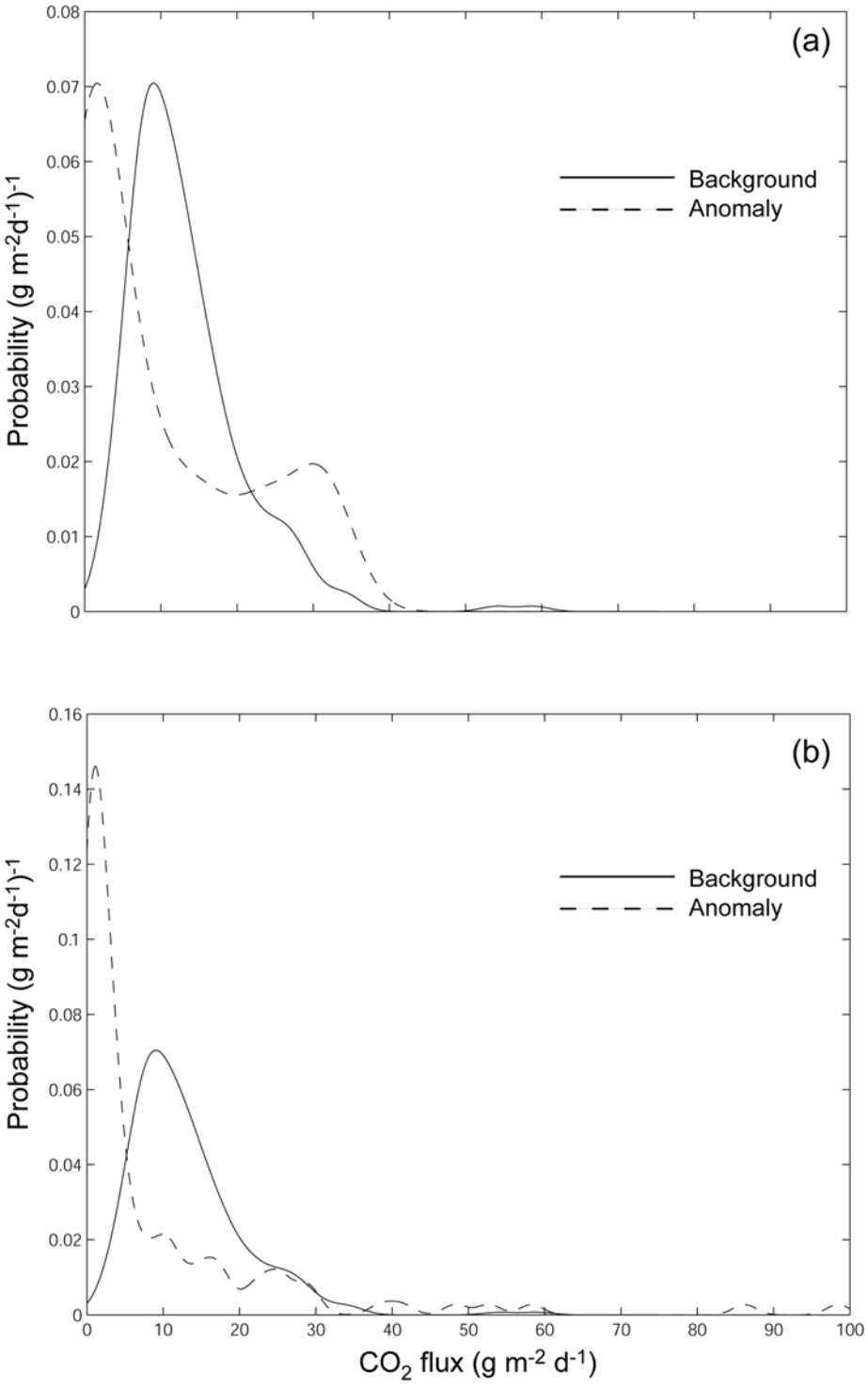

Figure 7.2. Probability density functions of background central California soil CO_2 flux and anomalous CO_2 flux associated with (a) homogeneous isotropic (see Figure 4.9 for surface CO_2 flux profile associated with high source geothermal CO_2 flux) and (b) heterogeneous isotropic (see Figure 4.12 for surface CO_2 flux profile associated with high source geothermal CO_2 flux) permeability structures.

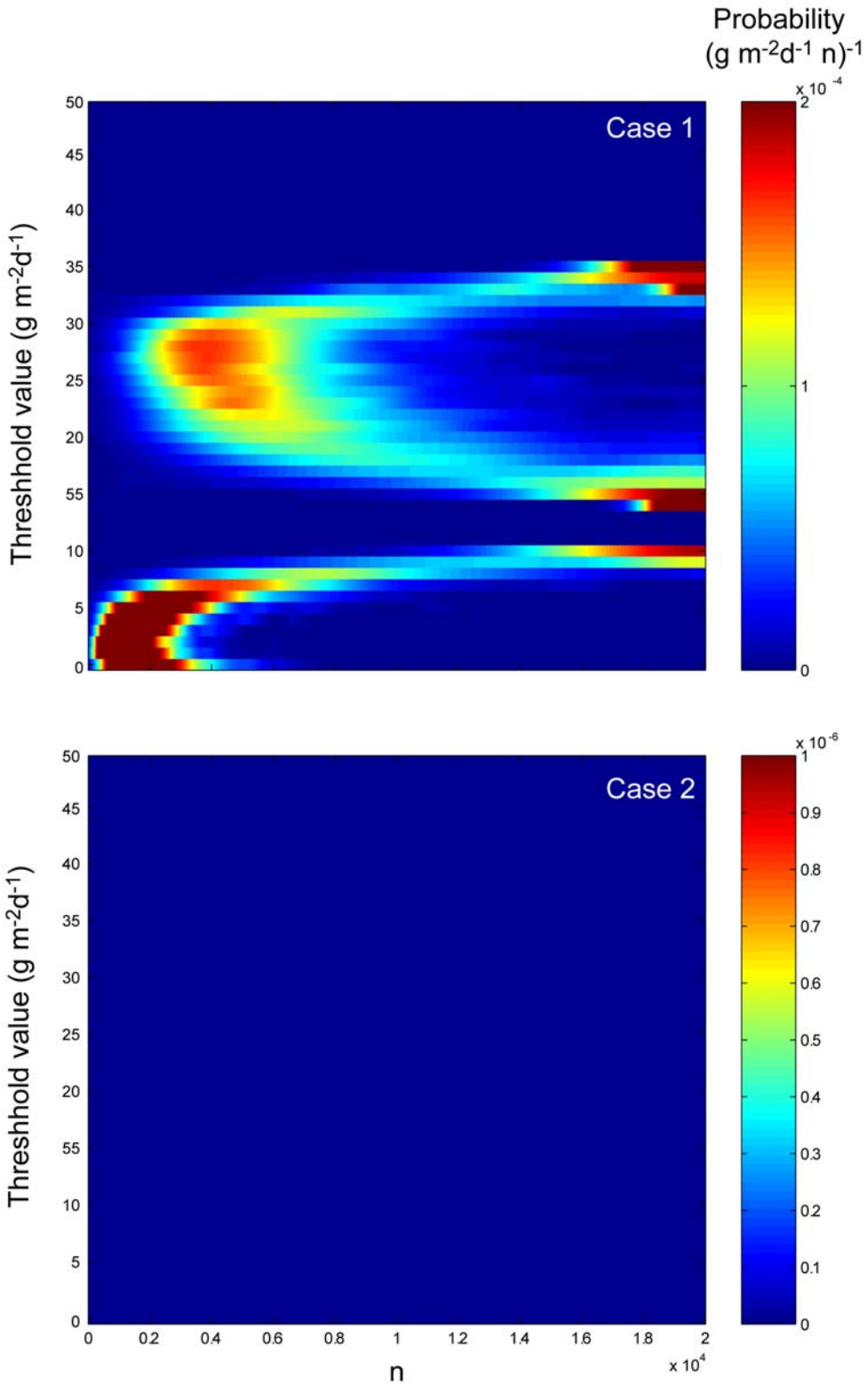

Figure 7.3. Probability image plots for Cases 1 and 2 Monte Carlo simulations (see Table 7.2).

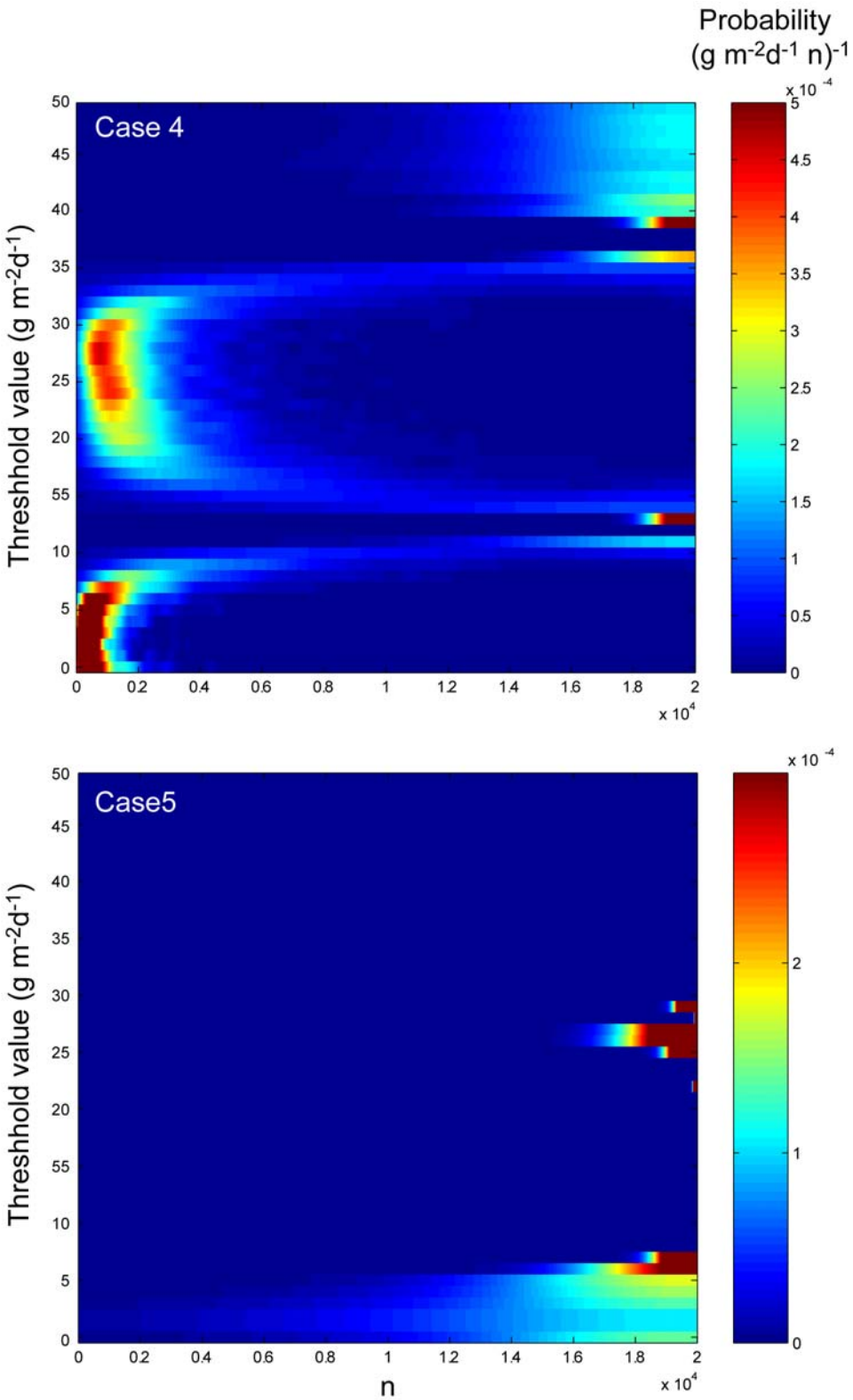

Figure 7.4. Probability image plots for Cases 4 and 5 Monte Carlo simulations (see Table 7.2).

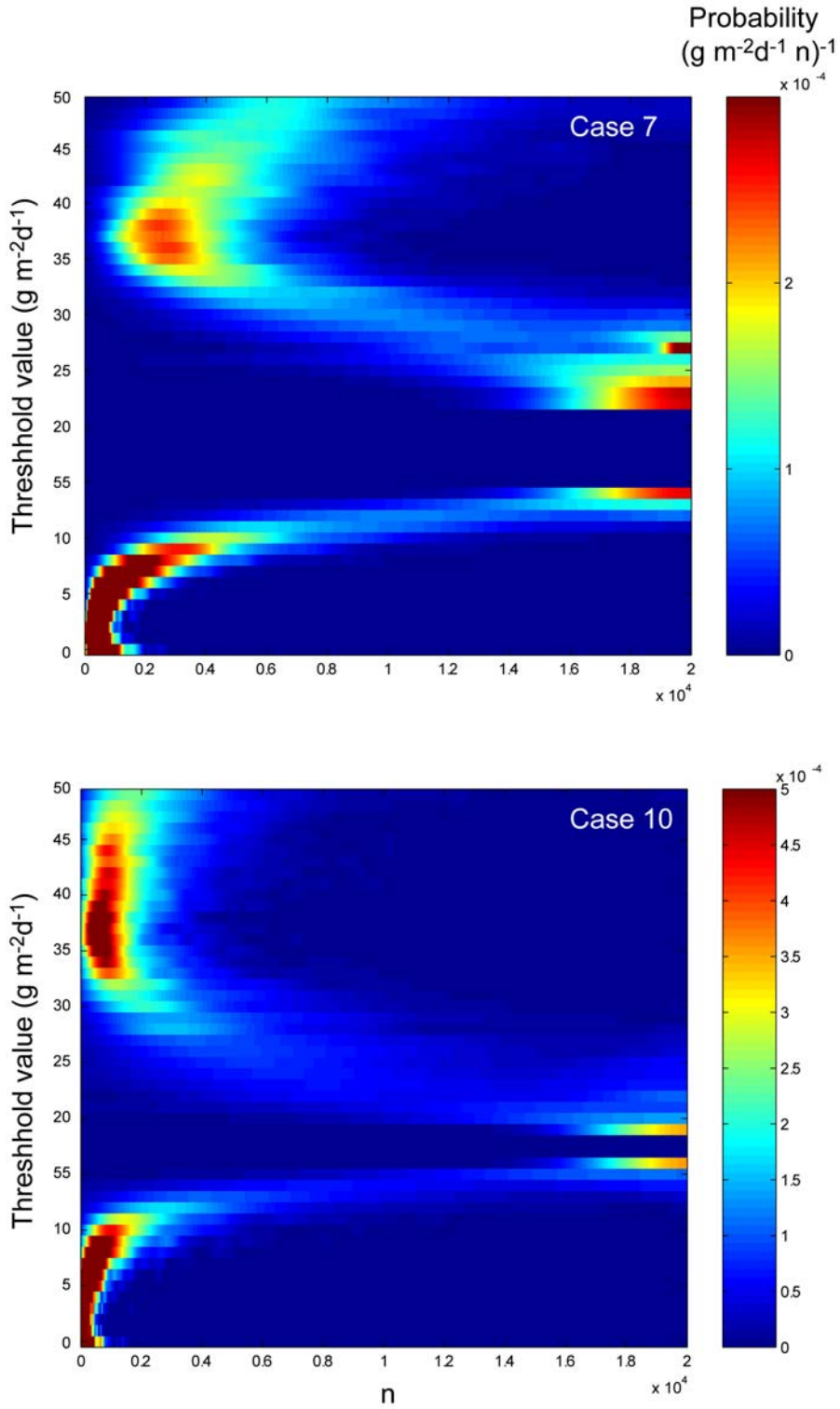

Figure 7.5. Probability image plots for Cases 7 and 10 Monte Carlo simulations (see Table 7.2).

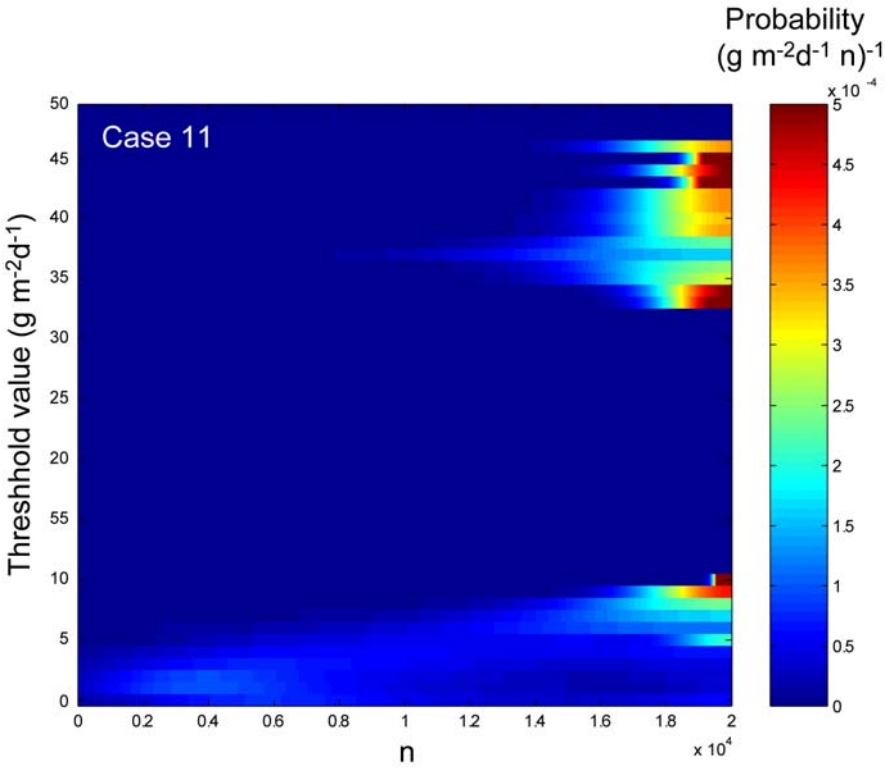

Figure 7.6. Probability image plots for Case 11 Monte Carlo simulation (see Table 7.2).